Construction and Building Materials 542 (2026) 147963

Contents lists available at ScienceDirect

Construction and Building Materials

journal homepage: www.elsevier.com/locate/conbuildmat

Chloride-induced corrosion initiation of carbon steel in sulfide-containing cementitious environments

Ali Nikoonasab [a,b], Thoralf Müller [c], Michael Raupach [b], Gregor J.G. Gluth [a,*]

[a] Division 7.4 Technology of Construction Materials, Bundesanstalt für Materialforschung und -prüfung (BAM), Unter den Eichen 87, Berlin 12205, Germany
[b] Institute for Building Materials Research (ibac), RWTH Aachen University, Schinkelstr. 3, Aachen 52062, Germany
[c] Division 7.6 Corrosion and Corrosion Protection, Bundesanstalt für Materialforschung und -prüfung (BAM), Unter den Eichen 87, Berlin 12205, Germany

ARTICLE INFO

Keywords:
Cement
Blast furnace slag
Steel corrosion
Sulfide
Redox conditions
Oxidation
Chloride

ABSTRACT

The mechanism and consequences of passivation and chloride-induced corrosion initiation of steel in systems with reduced sulfur species (HS^-, S_n^{2-}, $S_2O_3^{2-}$, SO_3^{2-}), including reinforcement corrosion in concrete, are insufficiently understood to date. In this context, the present study investigated the electrochemical behaviour of carbon steel in synthetic pore solutions simulating ground granulated blast-furnace slag (GGBFS)-containing concrete, with a focus on the combined effects of reduced sulfur species and chloride, under anoxic, oxic and fully oxidised conditions. A three-electrode cell configuration was employed to conduct electrochemical analyses, including measurements of open-circuit potential (OCP), polarisation resistance (R_p), and electrochemical impedance spectroscopy (EIS) to monitor passive film formation and stability. The critical chloride threshold (c_{crit}) for steel corrosion initiation was studied by incremental NaCl additions to the synthetic pore solutions; these solution-based values serve as upper-bound estimates for steel embedded in concrete. In sulfide-containing solutions, steel did not passivate before complete oxidation of the reduced sulfur species, exhibiting OCP values of −550 to −700 $mV_{Ag/AgCl}$ and R_p values of 3–50 $k\Omega \cdot cm^2$. No corrosion initiation occurred up to 4 M chloride in solutions containing $\geq$ 50 mM HS^-, even after oxygen exposure. The behaviour remained independent of pH because reduced sulfur species maintained anoxic conditions at the steel surface, with dissolved oxygen below the detection limit after days of air exposure. Passivation occurred only after complete oxidation of reduced sulfur species to sulfate, with R_p increasing to 65–145 $k\Omega \cdot cm^2$. The effect of reduced sulfur species is therefore transient and ends when the oxidation front reaches the reinforcement and oxidises all reduced sulfur species, a process that may take decades in some cases of GGBFS concretes, during which conventional corrosion criteria and the critical chloride threshold concept are not applicable to these systems.

1. Introduction

Reinforced concrete stands as the backbone of modern infrastructure globally, valued for its strength, versatility, and cost-effectiveness. However, the durability of reinforced concrete structures remains a critical concern in civil engineering, particularly when exposed to aggressive ions such as chlorides [1,2]. Corrosion of reinforced steel is the most common and costly form of reinforced concrete degradation, leading to cracking, spalling, loss of structural integrity, and potentially catastrophic failures. The economic impact is large, with estimates suggesting corrosion maintenance and repair costs represent a significant fraction of the Gross Domestic Product in industrialized nations [3]. While the corrosion behavior of steel in ordinary Portland cement (OPC) systems has been extensively studied [2,4,5], the electrochemical mechanisms in ground granulated blast-furnace slag (GGBFS)-containing concrete require further elucidation. This knowledge gap becomes particularly relevant because of the increasing use of GGBFS as a supplementary cementitious material (SCM) in blended cements and alkali-activated materials (AAMs) to improve concrete sustainability and durability. AAMs are produced by reacting an aluminosilicate precursor with an alkaline activator, yielding a calcium aluminosilicate hydrate gel and/or a sodium aluminosilicate hydrate gel [6]. Both GGBFS-blended cements and alkali-activated slag resist chloride ingress better than OPC, due to a refined, poorly connected pore network [7,8] and because of chloride binding by hydrotalcite-type layered double hydroxide phases [9–12].

* Corresponding author.
E-mail address: gregor.gluth@bam.de (G.J.G. Gluth).

https://doi.org/10.1016/j.conbuildmat.2026.147963
Received 29 June 2026; Received in revised form 5 August 2026; Accepted 23 August 2026
Available online 26 August 2026
0950-0618/© 2026 The Author(s). Published by Elsevier Ltd. This is an open access article under the CC BY license (http://creativecommons.org/licenses/by/4.0/).

Conventional corrosion studies have primarily focused on chloride-induced corrosion mechanisms of reinforced steel embedded in OPC concrete in aerobic conditions, establishing critical chloride thresholds (c_{crit}) and understanding the associated electrochemical reactions [13–15]. However, the complex chemistry of GGBFS-containing concrete pore solutions, characterized by reduced sulfur species (HS^-, S_n^{2-}, $S_2O_3^{2-}$, SO_3^{2-}) and reducing conditions [16–19], presents unique challenges that remained understudied.

Steel reinforcement, embedded in concrete made from OPC, is protected by the concrete's pore solution. This solution, highly alkaline due to cement hydration, enables the steel to spontaneously passivate, forming a thin (typically a few nanometers thick) and thermodynamically stable oxide layer on its surface [20–22]. This passive film acts as a crucial kinetic barrier, dramatically reducing the metal dissolution rate to very low values and effectively protecting the steel for decades. Consequently, the quality, composition, and stability of this passive film are fundamental determinants of reinforced concrete durability [20]. However, the formation and stability of passive films on steel in alkaline solutions containing reduced sulfur species differ fundamentally from conventional passivation. Studies have demonstrated that in the absence of oxygen, sulfide ions can participate in the formation of surface layers through the formation of iron sulfides (FeS, FeS_2) [23,24]. These sulfide-containing films exhibit distinct electronic properties compared to typical iron oxide passive layers, possessing higher conductivity and different defect structures that may compromise their protective capabilities [25,26]. Steel corrosion in sulfide-containing environments is not limited to GGBFS-containing cements but extends to other important industrial processes. Notable examples include the kraft process in the pulp industry and the oil and gas industry [24].

While recent investigations of steel in GGBFS-containing cements suggest improved resistance to chloride-induced corrosion compared to OPC [27–29], an alternative viewpoint suggests that under anoxic and sufficiently reducing conditions, the thermodynamic likelihood of forming iron sulfide phases, such as mackinawite or pyrrhotite, on the steel surface could result in porous, non-protective layers that reduce corrosion resistance of steel in such environments [26,30–33]. The presence of reduced sulfur species in concrete pore solutions creates a complex corrosion environment through sulfide oxidation reactions that consume dissolved oxygen, producing either partially oxidised intermediates such as polysulfides, thiosulfate, and sulfite, or fully oxidised sulfate species [16,19]. This oxygen depletion phenomenon exhibits contradictory effects on steel reinforcement corrosion: while it provides protection by limiting the primary cathodic oxygen reduction reaction (ORR) [24], it simultaneously creates detrimental conditions by inhibiting oxide formation on steel surfaces and eliminating the regeneration mechanism for protective oxide layers, thereby compromising the steel's natural passivation capacity [31]. Moreover, the presence of reduced sulfur species changes the response of steel to common electrochemical analytical methods, compared to the response of steel in OPC pore solutions, making current recommendations and thresholds to detect steel corrosion in concrete unreliable [34].

The internal environment of mature, water-saturated GGBFS-containing concrete is typically characterized by extremely low oxygen concentrations due to the slow diffusion of oxygen through dense, saturated concrete and its consumption by oxidation of reduced species, establishing anoxic or nearly-anoxic conditions [35–38]. Despite the widespread application of GGBFS-containing cements and the recognized significance of sulfide chemistry in these oxygen-depleted environments, substantial knowledge gaps remain regarding the combined effects of alkalinity, dissolved sulfides, and oxygen on reinforcing steel durability. Moreover, the impact of varying sulfide levels and oxygen ingress on steel's resistance to chloride attack, particularly regarding c_{crit}, remains largely unexplored, hindering the development of accurate service life prediction models for GGBFS concrete structures.

To answer remaining questions, this study systematically investigated the effect of sulfide concentration in simulated cement pore solutions on the electrochemical behavior of carbon steel under both anoxic and oxic conditions. The analyses include monitoring the surface film formation on steel over time using electrochemical measurements in simulated pore solutions with varying sulfide concentrations and determining the critical chloride threshold (c_{crit}) for steel corrosion initiation through incremental chloride addition. Unlike previous studies performed at a single redox condition, this work uses the redox state as a controlled variable by investigating identical steel/solution systems under sulfide-containing anoxic conditions, sulfide-containing oxic (exposure to oxygen) conditions, and after complete oxidation of reduced sulfur species to sulfate, reproducing the progression of an oxidation front through the concrete cover. Additionally, the oxygen-scavenging effect of reduced sulfur species is directly quantified through dissolved oxygen measurements. A systematic sulfide concentration range (0–350 mM), obtained from pore solutions of hardened GGBFS-containing binders [19], is used instead of a single composition. By varying pH and sulfur redox state, this study identifies their effect on corrosion behaviour. This work thus contributes essential knowledge for predicting the long-term durability of steel reinforcement embedded in GGBFS-containing concrete structures.

2. Materials and methods

2.1. Carbon steel

The steel used in this study was S235JRG2 carbon steel with a chemical composition (in weight percent) of C: 0.17%, Si: 0.05%, Mn: 1.4%, S: 0.03%, P: 0.03%, and Fe: balance. Steel specimens were prepared by cutting and machining the material into disk-shaped electrodes, each possessing an exposed surface area of 0.4 cm^2. Before the electrochemical experiments, the surface of each steel specimen was cleaned using acetone followed by isopropyl alcohol. This cleaning procedure was implemented to remove potential surface contaminants and ensure a consistent, reproducible initial surface condition for all tests. A photograph of a representative steel specimen is provided in the Supplementary Information (Supplementary Fig. S1).

2.2. Synthetic pore solutions

Seven synthetic pore solutions were prepared using analytical-grade reagents NaOH, $Ca(OH)_2$, Na_2SO_4, NaCl, and commercial-grade $Na_2S{\cdot}xH_2O$ (x = 3.01, determined by thermogravimetry), based on literature data about the compositions of pore solutions expressed from hardened cement pastes [16,19]. Deionized water served as the solvent for all solutions; before its use in solution preparation, the deionized water was deaerated by purging with high-purity nitrogen gas (≥ 99.9995**)** for a duration of 30 min inside the glovebox. The effectiveness of this purging step was confirmed by measuring the residual dissolved oxygen concentration in the de-aerated water using a dissolved-oxygen sensor; the measured level was consistently below 0.2 ppm. This pre-conditioned water was then used to prepare all solutions inside a glovebox continuously flushed with high-purity nitrogen to prevent oxygen contamination during reagent addition and handling.

The compositions of the different synthetic pore solutions thus prepared are shown in Table 1, where each solution represents the

Table 1
Compositions of the synthetic cement pore solutions.

Solution	Na^+ (mM)	Ca^{2+} (mM)	SO_4^{2-} (mM)	S^{2-} (mM)
AAS100	1500	0.5	50	350
AAS90	1400	0.5	50	300
AAS75	1200	0.5	50	200
AAS50	800	0.5	50	50
CEM III	100	0.5	2	10
CEM III + Act	1000	0.5	200	100
CEM I	550	1	20	0

composition of a hardened cement paste or concrete based on a specific cement [19]. The synthetic pore solutions designated AAS approximate the pore solutions of concretes based on alkali-activated GGBFS with 100%, 90%, 75%, and 50% GGBFS in the solid binder, respectively, the remainder being hard coal fly ash. The pore solution CEM III represents the pore solution of a blast furnace cement (CEM III/B or CEM III/C according to European standard EN 197–1). Pore solution CEM III + Act represents the pore solution of a concrete based on a CEM III/C with the addition of 4% Na_2SO_4 as activator, a so-called 'hybrid cement' [19, 39–42]. Pore solution CEM I represents the pore solution of an OPC (CEM I according to EN 197–1), *i.e.*, a cement without GGBFS.

2.3. Electrochemical measurements

Electrochemical characterisation was performed using a Potentiostat/Galvanostat/ZRA Gamry Interface 1010E. All experiments were conducted at a laboratory temperature of 25 ± 2 °C. A standard three-electrode cell configuration was used. The setup contained the steel disk specimen as the working electrode (WE), a platinum sheet as the counter electrode (CE), and a saturated Ag/AgCl electrode serving as the reference electrode (RE). All given potentials in this paper are referred to the given saturated Ag/AgCl electrode ($E^{\circ}_{Ag/AgCl} = +0.197$ V *vs.* SHE). To ensure statistical validity and assess reproducibility, all electrochemical measurements for each condition (specific synthetic pore solutions, immersion time and chloride concentration) were conducted on a minimum of three independent replicate steel specimens. Before initiating any electrochemical sequence, each specimen, once immersed in the designated synthetic pore solutions within the cell, was allowed an initial stabilization period of 20 min at open circuit potential (OCP).

2.3.1. Monitoring in chloride-free solutions under anoxic conditions (passivation study)

The evolution of the steel surface state upon immersion in chloride-free synthetic pore solutions was monitored over a 14-day period. Measurements were conducted 2 h, 1 day, 7 days, and 14 days after immersion. To obtain a stable and representative value, the reported OCP was determined by averaging the potential readings over the final 50 s of 10 min of measurement. Following the OCP measurement, linear polarisation resistance (LPR) measurements were performed by applying ±5 mV potential difference around the measured OCP at a scan rate of 0.167 mV/s. This small perturbation ensures an approximately linear current response (assuming Tafel kinetics apply near OCP) and minimizes disturbance of the surface film. The slope of the resulting potential (E) vs. current (I) plot near OCP yields the polarization resistance (R_p), calculated according to

$$R_p = (\Delta E / \Delta I) \quad (1)$$

Electrochemical impedance spectroscopy (EIS) measurements were performed potentiostatically at the measured OCP for selected solutions after 14 days of immersion. A sinusoidal AC potential perturbation with an amplitude of 5 mV RMS (root mean square) was applied over a frequency range from 100 kHz to 10 mHz, and 10 points per decade of frequency were recorded. The resulting impedance spectra were analysed by fitting to suitable equivalent electrical circuit (EEC) models using the *Gamry Echem Analyst* software to extract parameters related to the solution resistance, charge transfer resistance, and surface film properties.

Potentiodynamic anodic polarization scans were performed after 14 days of immersion to characterize the passive behavior in the chloride-free solutions. The potential was scanned in the anodic direction starting from OCP up to 1 V above OCP at a scan rate of 1 mV/s.

All experiments were conducted in a cell with continuous nitrogen purging to maintain anoxic conditions.

2.3.2. Anoxic and oxic chloride addition study (chloride threshold determination)

A separate set of experiments was conducted to specifically determine the critical chloride concentration required to initiate corrosion under sustained anoxic and oxic conditions. For this, steel specimens were first treated ('pre-passivated') by immersion in the chloride-free synthetic pore solutions for a period of 10 days, ensuring the establishment of a stable surface layer under oxygen exclusion. Following this pre-passivation phase, controlled amounts of NaCl were incrementally added directly to the anoxic solution to achieve progressively higher chloride concentrations, *viz.*, 0.2 M, 0.4 M, 0.6 M, 0.8 M, 1 M, 1.5 M, 2 M, 2.5 M, 3 M, and 4 M. After each NaCl addition, the solution was gently stirred to ensure homogenization, and then the system was allowed to equilibrate for 2 h. This 2-hour equilibration period was considered sufficient based on preliminary results, which showed that OCP and R_p reached stable values within 2 h of each chloride increment in sulfide-containing solutions. After the equilibration period at each chloride level, the OCP was recorded, followed immediately by a LPR measurement. This cycle of chloride addition, equilibration, OCP recording, and LPR measurement was repeated until significant signs of corrosion initiation, *i.e.*, a large decrease of OCP, and a significant decrease of R_p [43] were observed, or the maximum chloride concentration was reached. The criterion for corrosion initiation was adopted from previous work in which it was established that the transition from passive to active state of reinforcing steel in concrete has occurred when the OCP decreased by at least 200 mV between successive measurements (usually within 6–12 h), and R_p recorded after that decrease dropped to below 40 kΩ·cm^2 [43]. Throughout the entire procedure to determine c_{crit}, anoxic conditions were maintained *via* continuous nitrogen purging of the cell headspace.

For oxic conditions, steel specimens were first pre-passivated under anoxic conditions in chloride-free synthetic pore solutions for 10 days, as for the above experiments. Then, the cell was exposed to ambient air for 10 days. Following this phase, chloride was incrementally introduced following the same concentration sequence as above, and the steel response was measured as in the anoxic experiments. The process continued until either corrosion initiation was observed or the maximum chloride concentration was achieved.

The chloride concentration range used in this study (0.2–4.0 M) was selected to identify the depassivation threshold across all solutions rather than to represent a specific exposure condition. The maximum chloride concentration of 4.0 M was chosen to achieve a chloride to hydroxide ratio ($[Cl^-]/[OH^-]$) within the range reported to cause depassivation of carbon steel in cement-based materials [13]. Since synthetic pore solutions have no chloride-binding capacity, the reported concentrations represent free chloride and should be considered upper limits relative to reinforced concrete systems.

2.3.3. Chloride-induced corrosion under oxic conditions in fully oxidised (sulfate) solutions

Diffusion and dissolution of oxygen in the concrete pore solution, and its reaction with the reduced sulfur species will eventually lead to complete oxidation of the sulfur in the solution, *i.e.*, to complete transformation of the sulfur species to sulfate (SO_4^{2-}). To simulate the conditions when this 'oxidation front' has reached the steel reinforcement in concrete elements, experiments in which all sulfur is present as sulfate in the synthetic pore solutions were performed.

Steel specimens were initially pre-passivated for 10 days under anoxic conditions in chloride-free sulfide-containing synthetic pore solutions and were then transferred to fully oxidised (sulfate-containing) solutions. The compositions of the oxidised synthetic pore solutions are shown in Table 2. Immersion in these sulfate-containing solutions continued for an additional 10 days before chloride addition started. NaCl was incrementally added directly to the solution to achieve concentrations from 0.2 to 4 M, as in **Section 2.3.2**. After each NaCl addition, the solution was gently stirred to ensure homogenization, and

Table 2
Compositions of the fully oxidised synthetic cement pore solutions.

Solution	Na^+ (mM)	Ca^{2+} (mM)	SO_4^{2-} (mM)
AAS100	1500	0.5	400
AAS90	1400	0.5	350
AAS75	1200	0.5	250
AAS50	800	0.5	100
CEM III	100	0.5	12
CEM III + Act	1000	0.5	300
CEM I	550	1	20

then the system was allowed to equilibrate for at least 4 days before performing OCP and LPR measurements. This cycle of chloride addition, equilibration, OCP recording, and LPR measurement was repeated until significant signs of corrosion initiation were evident or the maximum chloride concentration was reached. EIS measurements were performed potentiostatically at the measured OCP for selected chloride-free solutions and selected 4 M chloride solutions.

2.3.4. Chloride-induced corrosion and influence of pH

To investigate the influence of pH, steel specimens were pre-passivated in chloride-free CEM I and AAS100 synthetic pore solutions of varying pH for 10 days. The pH of the solutions was controlled by varying the addition of NaOH (Table 3). After pre-passivation, chloride was introduced in incremental steps from 0.2 to 4.0 M, with each step followed by at least 4 days of equilibration prior to OCP and LPR measurements.

For fully oxidised conditions, specimens were initially pre-passivated in chloride-free, sulfide-containing solutions of varying pH for 10 days under anoxic conditions and were then transferred to fully oxidised (sulfate-containing) AAS100 solutions of the same pH, shown in Table 3. After a further 10 days of immersion, chloride was introduced incrementally following the usual concentration sequence. In this case, the equilibration period after each addition was a minimum of 2 days before conducting OCP and LPR measurements. EIS analyses were performed at OCP for selected chloride-free and 4 M chloride solutions.

2.4. pH-E_h-M diagrams (3D Pourbaix diagram)

The pH-E_h-M diagrams for the Fe-H_2O and Fe-S-H_2O systems at 298 K and 1 atm were constructed through custom programming with the *Wolfram Mathematica* software. For the Fe-H_2O system, a pH-E_h-M diagram was generated with variable iron concentration. For the Fe-S-H_2O system, the total dissolved iron concentration was fixed at 10^{-6} M, while sulfur concentration varied from 10^{-3} to 0.5 M, creating a pH-E_h-M three-dimensional representation. For the construction of the diagrams, the concentrations of the dissolved species were considered, *i.e.*, activity coefficients were not calculated, consistent with an idealised approach for Pourbaix diagram construction. Standard electrode potentials (E°) required for the Nernst equation were calculated using thermodynamic data (standard Gibbs free energies of formation) obtained from the IUPAC compilation [44]. All potentials were converted from the standard hydrogen electrode (SHE) to the Ag/AgCl reference electrode scale ($E^\circ_{Ag/AgCl}$ = +0.197 V *vs.* SHE) to match the present experimental conditions. Thermodynamic equilibrium boundaries between species were calculated using the Nernst equation, considering activity-pH-potential relationships for relevant aqueous species and solid phases. Water stability limits (H_2O/O_2 and H_2O/H_2) were incorporated to delineate the thermodynamically stable aqueous region. Interactive 3D plots are provided as Supplementary Information 2 and 3 (for details, see Supplementary Note 1).

Table 3
Compositions of the synthetic cement pore solutions with varied pH values.

Solution	Na^+ (mM)	Ca^{2+} (mM)	SO_4^{2-} (mM)	S^{2-} (mM)
AAS100 pH 13.8	1500	0.5	50	350
AAS100 pH 13.2	957.5	0.5	50	350
AAS100 pH 12.7	849.1	0.5	50	350
AAS100 pH 13.8 (fully oxidised)	1500	0.5	400	0
AAS100 pH 13.2 (fully oxidised)	957.5	0.5	400	0
AAS100 pH 12.7 (fully oxidised)	849.1	0.5	400	0
CEM I pH 13.7	550	1	20	0
CEM I pH 13.2	196.5	1	20	0
CEM I pH 12.7	88.1	1	20	0
CEM I pH 12.2	53.9	1	20	0

3. Results

3.1. Electrochemical behaviour under anoxic, chloride-free conditions

The evolution of OCP and R_p during the 14-day exposure period in anoxic, chloride-free solutions is presented in Fig. 1. The initial, moderate change in OCP and R_p observed for some of the specimens upon immersion is likely due to the non-equilibrium state of the steel surface at the moment of first contact with the anoxic electrolyte. Throughout the exposure, steel in the CEM I synthetic pore solution consistently exhibited much more positive OCP values than those in any of the sulfide-containing systems. Initially, the OCP for steel in CEM I was about −250 $mV_{Ag/AgCl}$, rising to approx. −150 $mV_{Ag/AgCl}$ by day 14. It is noted that these OCP values are more positive than the thermodynamic stability limit of water (approx. −1000 $mV_{Ag/AgCl}$) typically observed in strictly anoxic concrete [45,46]. This indicates that the OCP in the CEM I reference solution was influenced by trace levels of dissolved oxygen resulting from the solution handling and experimental setup. Conversely, all sulfide-containing systems showed persistently negative OCP values, generally between −550 and −700 $mV_{Ag/AgCl}$, with only minor change over the two weeks and small differences across the range of sulfide concentrations. Specifically, steel in CEM III solutions with the lowest sulfide levels exhibited OCPs near −550 $mV_{Ag/AgCl}$, whereas those in CEM III + Act and all AAS solutions were grouped between −650 and −700 $mV_{Ag/AgCl}$.

The LPR measurements revealed distinct differences between cement systems. Steel specimens in CEM I solution demonstrated higher polarization resistance, with R_p ranging from ~70 kΩ·cm^2 to ~250 kΩ·cm^2 by day 14, indicating decreasing corrosion rates over time. All sulfide-based systems exhibited variable but generally low R_p values, typically in the range 3–50 kΩ·cm^2. The electrochemical measurements clearly distinguished the corrosion behaviour of steel in CEM I from that in GGBFS-containing cementitious systems under anoxic conditions. Notably, even though steel specimens in the sulfide solutions exhibited low R_p values and very negative OCP values, which would usually be interpreted as indicating a high risk of corrosion, none of the steel samples displayed any visible signs of corrosion by the end of the exposure period.

Fig. 2 shows the anodic polarization curves of steel specimens in various synthetic pore solutions under anoxic conditions. The CEM I solution exhibited the most favourable conditions for steel passivation. The polarization curve shows a distinct transition from active iron dissolution (OCP up to ~300 $mV_{Ag/AgCl}$) to a passive region (approx. 300–600 $mV_{Ag/AgCl}$), followed by the onset of transpassive behaviour. Within the passive region, the current density remained approximately constant, indicating the formation of a stable and protective passive film on the steel surface. In contrast, the specimen in the CEM III solution containing a low concentration of sulfide displayed a reduction in OCP (to approx. −580 $mV_{Ag/AgCl}$) and exhibited higher current densities in potential range from −580 to + 250 $mV_{Ag/AgCl}$, approximately one order of magnitude greater than CEM I. Although some passivation behaviour was observed, it was significantly less pronounced than in the CEM I system, suggesting a less stable passive layer. Specimens in AAS

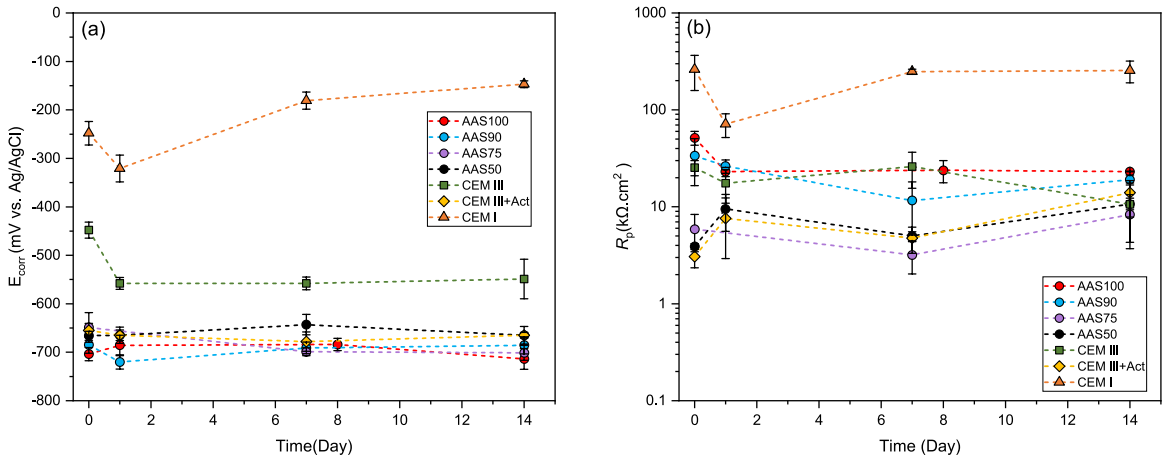


Fig. 1. Evolution of (a) the OCP and (b) the R_p of steel immersed in synthetic pore solutions under anoxic conditions.

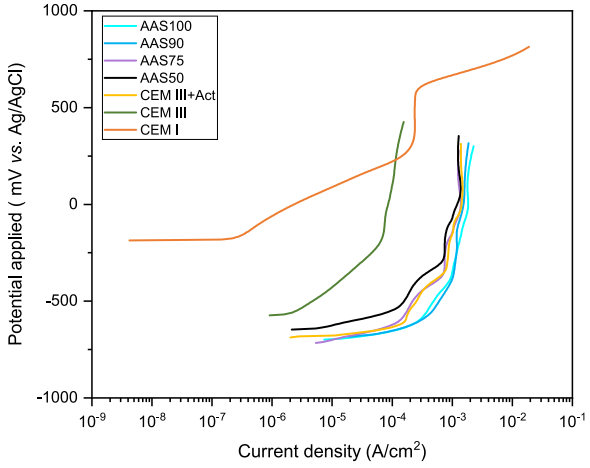


Fig. 2. The anodic polarization behaviour of steel in synthetic pore solutions under anoxic conditions.

100, 90, 75, 50, and CEM III + Act solutions exhibited significantly lower OCP values and higher current densities compared to the CEM I specimen. In these systems, the anodic curves lacked clearly identifiable active and passive regions and instead demonstrated characteristics of pseudo-passivation, indicating the absence of a stable and protective passive film under these conditions.

Fig. 3 show the electrochemical impedance behaviour of steel specimens after 14 days of pre-immersion in solutions with varying sulfide concentrations. The EIS measurements were conducted based on prior OCP and LPR analyses, focusing on selected systems with differing sulfide concentrations: high sulfide concentration (AAS100), medium sulfide concentration with elevated sulfate content (CEM III+Act), low sulfide concentration (AAS50), very low sulfide concentration (CEM III), and the sulfide-free reference (CEM I).

Fig. 4 illustrates the employed equivalent electrical circuit (EEC), which consists of two time constants, a configuration commonly applied to represent electrochemical behaviour in simulated concrete pore solutions [47–50]. In this model, the ideal capacitor is replaced by a constant phase element (CPE) to account for surface heterogeneity of the steel. The CPE provides a mathematical approximation of the impedance response, with its impedance Z_{CPE} defined by Eq. (2).

$$Z_{CPE} = Y_0^{-1} (j\omega)^{-n} \quad (2)$$

In this expression, Y_0 denotes the admittance related to a purely capacitive electrode (S·s^n. cm^{-2}), j is the imaginary unit, ω is the angular frequency (rad/s), and the exponent n characterises the deviation from ideal capacitive behavior. Depending on the value of n, the CPE can behave as an inductor ($n = -1$), a resistor ($n = 0$), or an ideal capacitor ($n = 1$). In the model, R_s is the solution resistance, R_{ct} is the charge transfer resistance, CPE_{dl} represents the constant phase element standing for the double layer capacitance, R_f and CPE_f reflect the properties of the passive layer and corrosion products formed on the steel surface, respectively. This EEC model is consistently applied to fit and interpret all EIS results presented throughout this study. The Kramers-Kronig transform was applied to the EIS data to assess the validity and self-

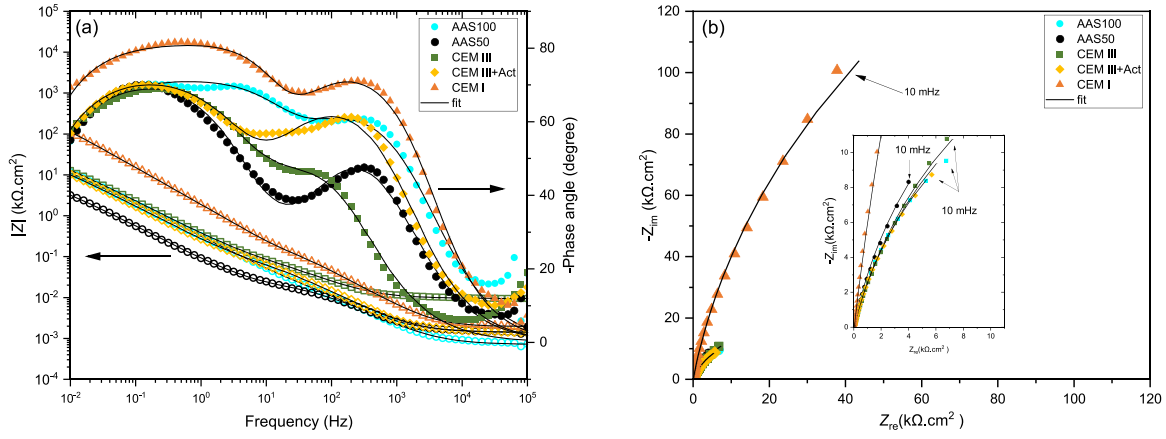


Fig. 3. The EIS responses of steel in synthetic pore solutions under anoxic conditions: (a) Bode plots and (b) Nyquist plots.

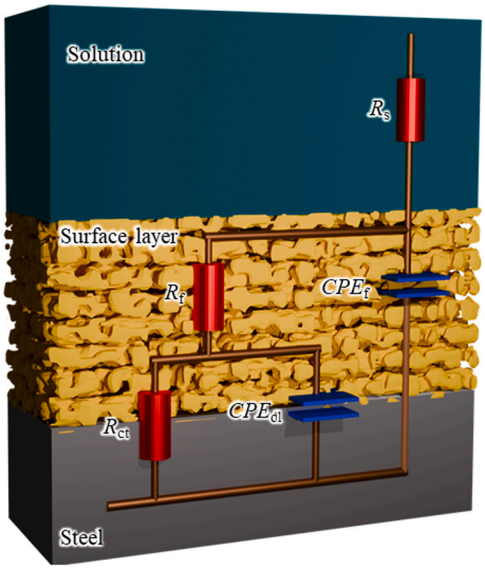


Fig. 4. Electrical equivalent circuit used for fitting the EIS data.

consistency of the measured spectra prior to fitting. This approach ensures that the impedance data satisfy the fundamental requirements of linearity, causality, and stability, confirming that the results are reliable and suitable for further analysis [51].

The Nyquist plot (Fig. 3**(b)**) reveals distinct electrochemical behaviours of sulfide-containing systems *versus* the sulfide-free system. Table 4 shows the fitting parameters obtained from the equivalent electrical circuit. The high-frequency intercept corresponds to the solution resistance (R_s), which varies from 0.7 Ω·cm^2 (AAS100) to 9.4 Ω·cm^2 (CEM III). The subsequent impedance arc reflects the passive film resistance (R_f), with steel in CEM I displaying the highest value of 374.8 Ω·cm^2 and AAS50 the lowest of 29.7 Ω·cm^2. At lower frequencies, the progression of the impedance values indicates the charge-transfer resistance (R_{ct}): steel in CEM I exhibits the highest R_{ct} at 479 kΩ·cm^2, while the other systems are in the range 35–45 kΩ·cm^2. Constant phase element parameters further clarify surface characteristics, with n_f ranging from 0.735 (CEM III) to 0.874 (CEM I) and n_{dl} from 0.806 (CEM III) to 0.971 (CEM I), highlighting the greater film uniformity achieved by CEM I relative to the other systems.

The Bode magnitude plot (Fig. 3**(a)**) displays the impedance behaviour across the measured frequency range (10^{-2} to 10^5 Hz). Steel in CEM I exhibits the highest impedance, peaking at approx. 10^2 kΩ·cm^2 at the lowest frequencies, which signals the formation of a highly resistive passive film. The sulfide-containing systems exhibit lower impedance values, with AAS50 around 1 kΩ·cm^2 at low frequency, indicating a less protective surface layer. The phase angles (Fig. 3**(a)**) exhibit two distinct maxima for all systems, corresponding to separate electrochemical processes at the steel/solution interface. For CEM I, the first peak at mid-high frequency is around 70°, while the second maximum at mid-low frequency reaches approx. 80°. This pattern indicates the formation of a compact and homogeneous passive film [47,48], with the high-frequency peak associated with surface film formation and modification, and the low-frequency peak linked to charge transfer. In contrast, AAS100 exhibits a first peak at mid-high frequency near 60° and a second maximum at mid-low frequency around 70°, while AAS50 shows a first peak at about 50° and a second maximum also near 70°. These lower phase angle values in the sulfide-containing systems suggest more heterogeneous and less protective surface films compared to CEM I.

Together, high charge-transfer resistance, large passive film resistance, and well-separated, high phase angle maxima for CEM I are consistent with a dense, uniform, and protective passive layer. In contrast, sulfide-containing systems exhibited lower impedance, more heterogeneous interfacial properties, and lower high-frequency phase angle maxima.

3.2. Influence of sulfide on chloride-induced corrosion initiation under anoxic conditions

Fig. 5 shows the evolution of the OCP and R_p of steel specimens immersed in synthetic pore solutions with varying chloride concentrations, aiming to identify the critical chloride threshold for corrosion initiation under anoxic conditions. Steel specimens immersed in CEM I solution, initially stabilised at an OCP of approx. −140 $mV_{Ag/AgCl}$ in the chloride-free solution, and subsequently the OCP remained approximately constant up to 0.6 M Cl^-. Beyond this threshold, the OCP decreased, reaching −400 $mV_{Ag/AgCl}$ at 4 M Cl^-, indicating progressive depassivation with increasing chloride concentration. Correspondingly, R_p for steel in CEM I pore solution started at ~160 kΩ·cm^2 and decreased beyond 0.6 M Cl^-, stabilising around 50 kΩ·cm^2 at chloride concentrations of 1.5 M and higher. In contrast, all steel specimens in sulfide-containing solutions exhibited substantially more negative OCPs that varied only slightly with chloride addition. Notably, the steel in the CEM III solution began at approx. –500 $mV_{Ag/AgCl}$ and decreased monotonically to approx. −630 $mV_{Ag/AgCl}$ at 4 M Cl^- without the abrupt OCP drops characteristic of passive film breakdown [13,43]. The R_p values of steel specimens in sulfide-containing solutions remained in the range of 20–50 kΩ·cm^2 across the entire chloride range, demonstrating no impact of chloride on the polarisation resistance for these systems.

The observation that no clear c_{crit} was observed in the sulfide-containing solutions can be explained by sulfide preventing stable passive film formation on the steel surface. Without a passive film, chloride cannot cause the typical breakdown seen in CEM I. However, the limited dissolved oxygen under anoxic conditions restricts the cathodic reaction, which limits the rate of iron dissolution. This produces a steady state where R_p values remain low (20–50 kΩ·cm^2) and OCPs stay negative, regardless of chloride concentration. The steel surface is not truly passive but also does not undergo rapid corrosion, maintaining instead a stable low corrosion rate.

3.3. Oxygen scavenging by sulfide and its effect on chloride-induced corrosion initiation

Fig. 6 shows the OCP and R_p of steel specimens immersed in synthetic pore solutions during the pre-treatment phase and subsequent exposure to oxygen at varying chloride concentrations. The access of oxygen had a pronounced impact on both OCP and R_p, highlighting its dual role in

Table 4
Fitting parameters obtained from EIS of steel in synthetic pore solutions under anoxic conditions.

ID	R_s (Ω·cm^2)	R_f (Ω·cm^2)	$Y_{0\,f}$ (μS·s^n. cm^{-2})	n_f	R_{ct} (kΩ·cm^2)	$Y_{0\,dl}$ (μS·s^n. cm^{-2})	n_{dl}	χ^2
AAS 100	0.7	72.6	564.1	0.781	42.5	160.8	0.864	0.005
AAS 50	1.3	29.7	333.3	0.806	44.1	702.6	0.860	0.001
CEM III	9.4	42.3	689.7	0.735	44.5	628.2	0.806	0.004
CEM III + Act	1.4	123.3	402.6	0.803	36.0	448.7	0.827	0.003
CEM I	1.9	374.8	77.4	0.874	479.7	22.7	0.971	0.001

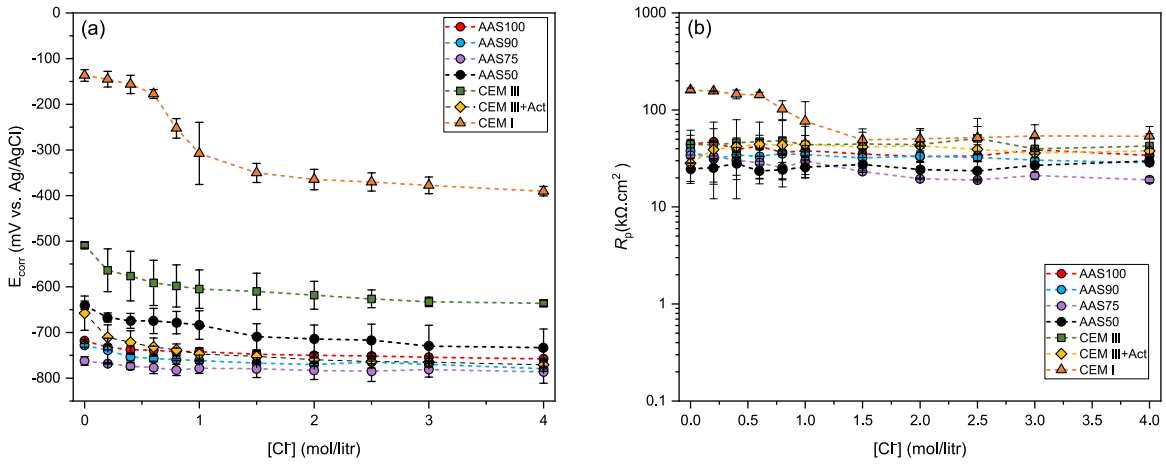


Fig. 5. Evolution of (a) OCP and (b) R_p of steel immersed in synthetic pore solutions as a function of chloride concentration under anoxic conditions.

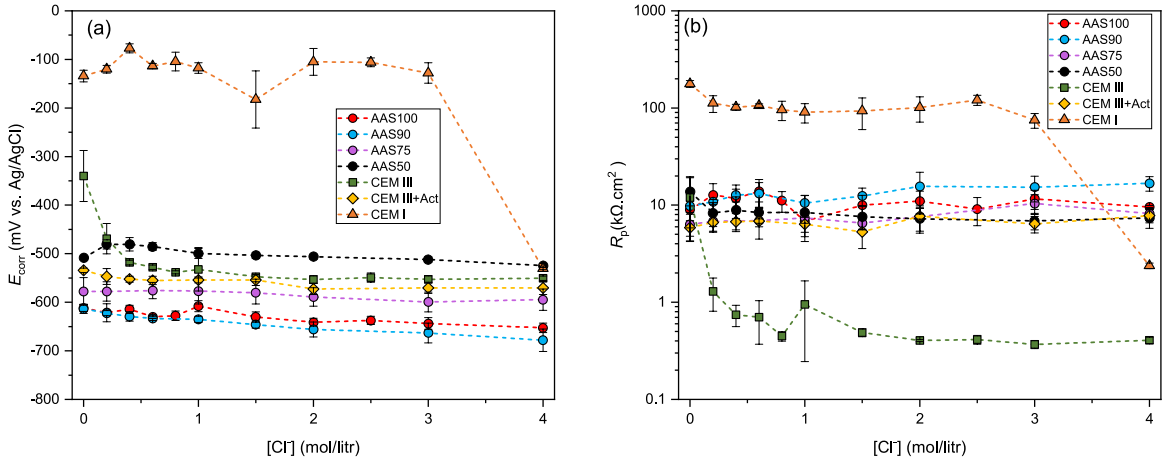


Fig. 6. Evolution of (a) OCP and (b) R_p of steel immersed in synthetic pore solutions with oxygen access as a function of chloride concentration.

promoting passive film formation and enabling film deterioration under chloride-induced corrosion conditions. Before chloride addition, steel specimens in the CEM I solution exhibited an OCP of approx. −130 $mV_{Ag/AgCl}$ and a high R_p of ~180 kΩ·cm^2. In contrast, steel in CEM III stabilised at −340 $mV_{Ag/AgCl}$ (R_p ~12 kΩ·cm^2), AAS 50 at −510 $mV_{Ag/AgCl}$ (R_p ~14 kΩ·cm^2), AAS 75 at −580 $mV_{Ag/AgCl}$ (R_p ~6 kΩ·cm^2), AAS 90 at −610 $mV_{Ag/AgCl}$ (R_p ~10 kΩ·cm^2), and AAS 100 at −610 $mV_{Ag/AgCl}$ (R_p ~10 kΩ·cm^2).

Upon change to oxic conditions and the first chloride increment to 0.2 M, CEM III exhibited an instantaneous decrease of R_p to approx. 1 kΩ·cm^2, accompanied by a 130-$mV_{Ag/AgCl}$ drop of OCP, indicating rapid depassivation/corrosion initiation [13,43]. Further chloride increments sustained steel specimens immersed in CEM III solution in an active corrosion regime (R_p at approx. 0.5–1 kΩ·cm^2). In contrast, steel specimens immersed in CEM I solution maintained relatively noble OCP values and R_p > 90 kΩ·cm^2 up to 3 M Cl^-, beyond which their OCP sharply decreased to −530 $mV_{Ag/AgCl}$ and R_p decreased to ~2 kΩ·cm^2, marking its c_{crit}.

Steel specimens in the AAS and CEM III + Act solutions exhibited stable OCP and R_p values across the entire chloride concentration range up to 4 M, with no significant shifts observed. This electrochemical behaviour correlates with the dissolved oxygen (DO) measurements presented in Table 5. DO concentrations were assessed both before NaCl addition (after 1 h of air bubbling) and after 7 days of exposure in 4 M chloride solution. The DO levels for CEM I and CEM III solutions ranged between 5.1 and 6.2 ppm, demonstrating oxygen availability, whereas all AAS solutions and the CEM III + Act solution exhibited no detectable oxygen at either time point. The absence of detectable dissolved oxygen in AAS and CEM III + Act solutions indicates that sulfide rapidly consumes dissolved oxygen through formation of thiosulfate sulfite etc. The

Table 5
Dissolved oxygen concentration of the synthetic pore solutions.

Solution	Dissolved oxygen concentration after 1 h of air bubbling (ppm)	Dissolved oxygen concentration after 7 days in 4 M chloride solution (ppm)
AAS 100	0	0
AAS 90	0	0
AAS 75	0	0
AAS 50	0	0
CEM III	5.1	6.2
CEM III + Act	0	0
CEM I	5.8	5.6

sulfide concentration is sufficient to scavenge oxygen continuously, maintaining anoxic conditions at the steel surface even after air exposure.

3.4. Chloride-induced corrosion initiation in fully oxidised (sulfate) solutions

The electrochemical behaviour of steel specimens in fully oxidised (sulfate) solutions with access of oxygen and increasing chloride concentrations was characterised by measuring their OCP and R_p after an initial 10-day immersion in sulfide-containing solutions, as shown in Fig. 7. Steel in CEM I solution is not included in this analysis, as no initial state in sulfide-containing solution exists in this case. Steel specimens in all AAS solutions showed stable OCP values ranging between −100 $mV_{Ag/AgCl}$ and −200 $mV_{Ag/AgCl}$, accompanied by R_p values around 100 $k\Omega{\cdot}cm^2$ across the full range of chloride concentrations, with no abrupt changes observed. In contrast, specimens in the CEM III solution stabilised at an OCP of −60 $mV_{Ag/AgCl}$ and an R_p of 130 $k\Omega{\cdot}cm^2$ in chloride-free conditions. The addition of 0.2 M chloride resulted in a sharp decrease in potential to −550 $mV_{Ag/AgCl}$ and a corresponding drop in R_p to 2 $k\Omega{\cdot}cm^2$. With further increases in chloride concentration, the OCP remained in the range of −530 and −570 $mV_{Ag/AgCl}$ while R_p gradually declined to approx. 1 $k\Omega{\cdot}cm^2$ at 4 M chloride. Steel specimens in the CEM III + Act solution maintained OCP values between −100 $mV_{Ag/AgCl}$ and −160 $mV_{Ag/AgCl}$ and R_p values between 80 $k\Omega{\cdot}cm^2$ and 100 $k\Omega{\cdot}cm^2$ up to 2.5 M chloride. At 3 M chloride, the potential decreased to −410 $mV_{Ag/AgCl}$ with an R_p of approx. 15 $k\Omega{\cdot}cm^2$, and at 4 M chloride, the OCP decreased further to −490 $mV_{Ag/AgCl}$ and R_p decreased to around 3 $k\Omega{\cdot}cm^2$.

The measurements reveal that after sulfide oxidation, the steel specimens show solution-dependent responses to chloride. CEM III showed immediate corrosion initiation at 0.2 M chloride, while CEM III + Act resisted corrosion up to 2.5 M chloride. All AAS solutions provided sustained passive protection throughout the tested range, maintaining R_p values around 100 $k\Omega{\cdot}cm^2$ and stable OCP values between −100 $mV_{Ag/AgCl}$ and −200 $mV_{Ag/AgCl}$, demonstrating superior chloride resistance compared to the low-slag cementitious environments for the chloride concentrations and exposure durations in the present study.

The EIS measurements (Fig. 8) reveal fundamental differences in passive film quality and stability among the tested systems. Table 6 presents the fitting parameters derived from the equivalent electrical circuit. Steel in the chloride-free CEM I solution showed high charge transfer resistance (R_{ct} = 413 $k\Omega{\cdot}cm^2$) and phase angle maxima of approx. 65° and 75°, indicating the formation of a highly protective, compact passive film. The addition of 4 M chloride to CEM I and CEM III solutions resulted in substantially lower impedance values (approx. 2 $k\Omega{\cdot}cm^2$ at low frequencies) and reduced phase angle maxima (30° to 40° at low frequencies), confirming passive film breakdown and the onset of active corrosion. In contrast, AAS100 and AAS50 systems exhibited similar impedance values (20–30 $k\Omega{\cdot}cm^2$) and phase angle maxima of approx. 60° to 75° both in chloride-free conditions and after addition of 4 M chloride. These results demonstrate that steel in AAS fully oxidised solutions retained a stable, protective passive film even at high chloride concentrations, whereas passive films in CEM I and CEM III undergo chloride-induced corrosion.

3.5. Influence of pH on chloride-induced corrosion initiation under anoxic and oxic conditions

The influence of pore solution chemistry (pH and anoxic vs. oxic) on the chloride-induced corrosion initiation of steel was investigated by varying the pH and the dominant sulfur anion (sulfide vs. sulfate) in synthetic solutions simulating CEM I and AAS100. In the CEM I system, a direct relationship was observed between pH and c_{crit} under oxic conditions, as has been established earlier [13,21,52,53].

The EIS measurements (Fig. 9) and the equivalent circuit fitting parameters (summarized in Table 7**)** demonstrate the influence of pH on passive film quality in CEM I solutions. Steel in solution with pH = 13.7 exhibited the highest charge transfer resistance (R_{ct} = 413 $k\Omega{\cdot}cm^2$), impedance at low frequencies (approx. 30 $k\Omega{\cdot}cm^2$), and phase angle maximum (approx. 77°), indicating the formation of a dense, protective passive film with near-ideal capacitive behavior. As pH decreased to 12.7 and 12.2, the electrochemical parameters deteriorated significantly: R_{ct} values decreased to 11 and 16.5 $k\Omega{\cdot}cm^2$, low-frequency impedance decreased to approx. 2 $k\Omega{\cdot}cm^2$, and phase angle maxima decreased to about 45° and 35°, respectively. The R_f also decreased from 733 $\Omega{\cdot}cm^2$ at pH = 13.7 to 89 $\Omega{\cdot}cm^2$ at pH = 12.2. These results confirm that a lower pH result in more heterogeneous, less protective surface films, underscoring the critical role of alkalinity in maintaining steel passivity in CEM I pore solutions.

The Nyquist and Bode plots for steel specimens in AAS100 solutions (Fig. 10) illustrate varied electrochemical responses depending on pH and sulfur species. As detailed in Table 8, steel in fully oxidised solutions exhibited different electrochemical responses compared to sulfide-containing solutions at equivalent pH values. At lower frequencies, the R_{ct} for the steel in fully oxidised solutions is 244 $k\Omega{\cdot}cm^2$ at pH = 13.2 and 152 $k\Omega{\cdot}cm^2$ at pH = 13.8. In contrast, for steel in sulfide-containing solutions, R_{ct} values are lower, 4 $k\Omega{\cdot}cm^2$ at pH = 13.2 and 42 $k\Omega{\cdot}cm^2$ at pH = 13.8. Additionally, in sulfide-containing solution at pH 12.7, the

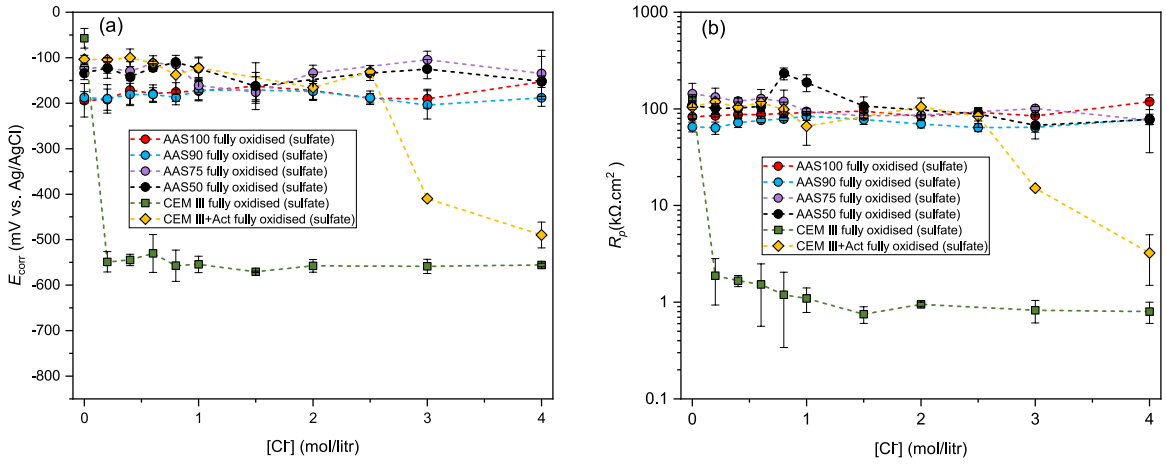


Fig. 7. Evolution of (a) OCP and (b) R_p of steel immersed in fully oxidised synthetic pore solutions as a function of chloride concentration under oxic conditions (oxygen access).

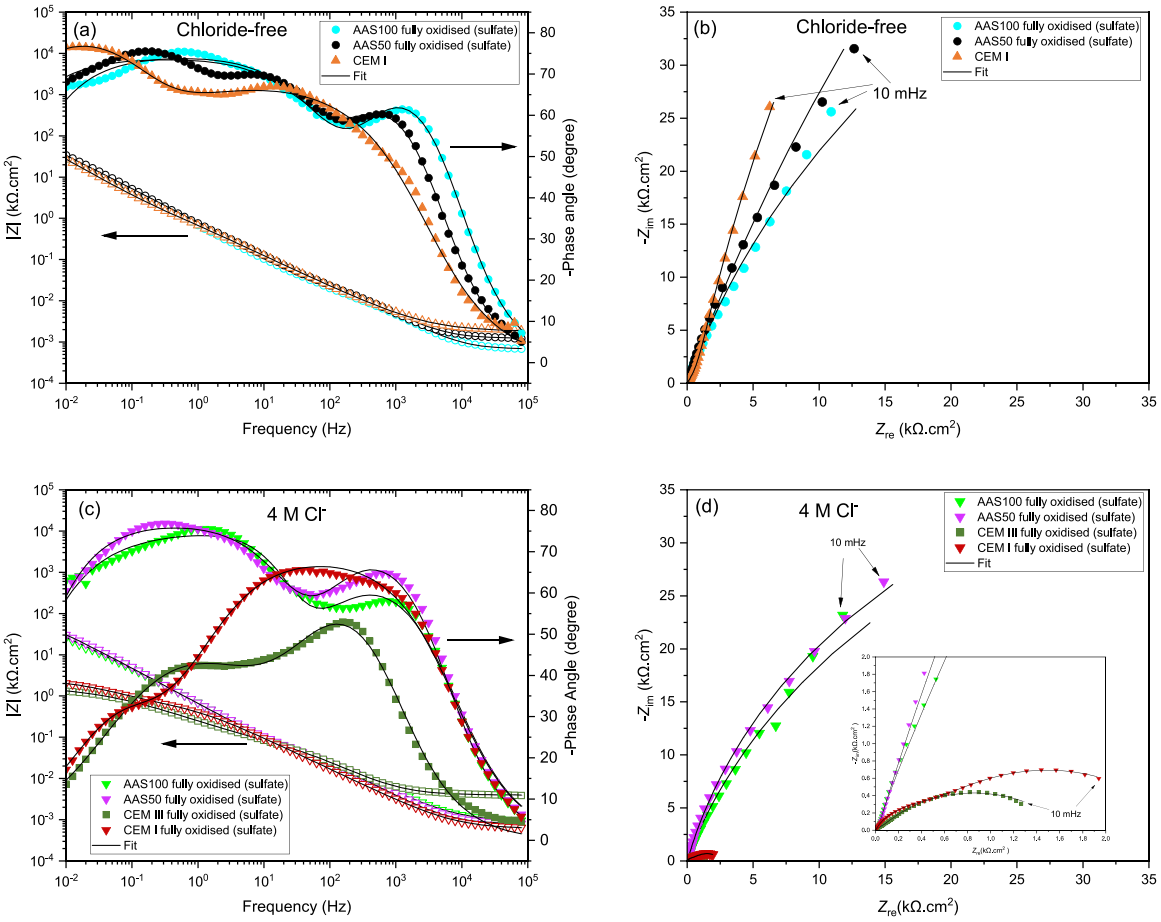


Fig. 8. The EIS responses for steel specimens in fully oxidised synthetic pore solutions under oxic conditions (oxygen access): (a) Bode plots and (b) Nyquist plots in chloride-free solutions, (c) Bode plots and (d) Nyquist plots in 4 M Cl^- solutions.

Table 6
Fitting parameters obtained from EIS of steel in various fully oxidised synthetic pore solutions under oxic conditions.

ID	R_s ($\Omega \cdot cm^2$)	R_f ($\Omega \cdot cm^2$)	$Y_{0\,f}$ ($\mu S \cdot s^n . cm^{-2}$)	n_f	R_{ct} ($k\Omega \cdot cm^2$)	$Y_{0\,dl}$ ($\mu S \cdot s^n . cm^{-2}$)	n_{dl}	χ^2
AAS 100 chloride-free	0.7	57.9	94.9	0.882	152.5	223.6	0.805	0.0006
AAS 100 4 M Cl^-	0.9	202.5	244.4	0.780	101.0	79.7	0.952	0.001
AAS50 chloride-free	1.2	99.1	113.8	0.862	425.1	167.4	0.795	0.001
AAS 50 4 M Cl^-	0.8	167.4	150.0	0.857	95.2	162.6	0.860	0.0005
CEM III 4 M Cl^-	4.0	81.5	208.5	0.810	1.6	1238.5	0.597	0.0006
CEM I chloride-free	1.8	733.2	771.8	0.680	413.4	443.6	0.903	0.0007
CEM I 4 M Cl^-	0.6	772.2	412.8	0.770	1.8	1979.5	0.712	0.0007

R_{ct} is 10 $k\Omega \cdot cm^2$, while in fully oxidised solution at the same pH, R_{ct} reaches 2 $k\Omega \cdot cm^2$.

The Bode plots (Fig. 10**(a)**) further show that both impedance and phase angle behaviour vary with pH and sulfur species type. Steel in fully oxidised solutions at pH = 13.2 and 13.8 exhibits the highest impedance (around 30 $k\Omega \cdot cm^2$ at low frequencies) and phase angle peaks near 75°, suggesting more protective films. In contrast, sulfide-containing solutions generally produce lower impedance values (ranging from about 4 to 10 $k\Omega \cdot cm^2$) and slightly reduced phase angles (around 65–70°), with the lowest performance observed for steel in fully oxidised solution at pH = 12.7 (~ 2 $k\Omega \cdot cm^2$). The phase spectra typically show two peaks, one at mid-high frequencies and another at mid-low frequencies, with peak positions shifting depending on conditions. These patterns reflect the combined influence of pH and sulfur chemistry on passive film formation and stability in AAS100 pore solution.

As shown in Fig. 11, at the highest pH of 13.7, the steel specimen in CEM I exhibited a stable passive state, characterized by noble OCP (–70 to –150 $mV_{Ag/AgCl}$) and R_p greater than 90 $k\Omega \cdot cm^2$. The critical chloride threshold was determined to be between 3 M and 4 M Cl^-, at which point an abrupt decrease of the OCP to –530 $mV_{Ag/AgCl}$ and a corresponding decrease of R_p to approx. 2 $k\Omega \cdot cm^2$ signified the onset of active corrosion. Reducing the pH to 13.2 significantly lowered the system's tolerance to chlorides; here, c_{crit} was substantially lower, at a value between 0.6 M and 0.8 M Cl^-. At the lowest pH levels of 12.7 and 12.2, the steel

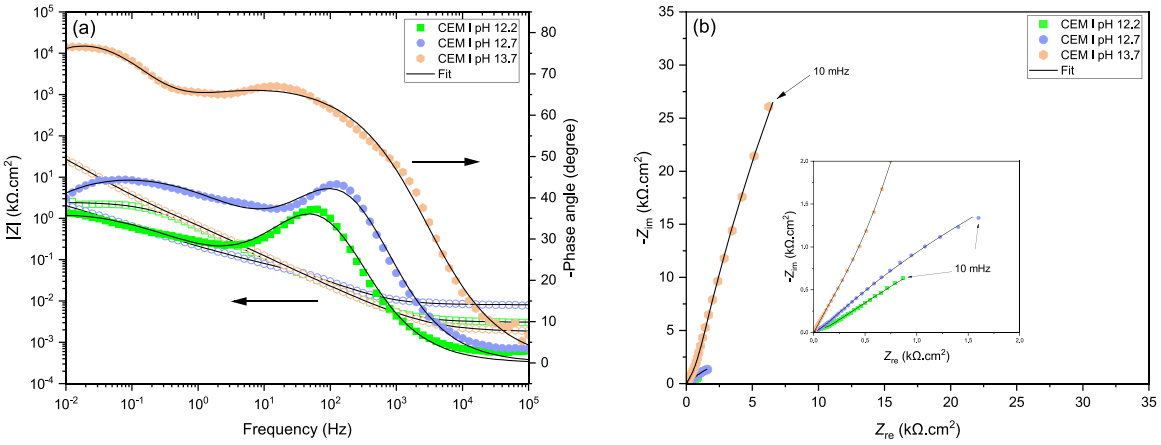


Fig. 9. The EIS responses of steel immersed in chloride-free CEM I solutions at different pH values: (a) Bode plots and (b) Nyquist plots.

Table 7
Fitting parameters obtained from EIS of steel in CEM I solutions at different pH values.

ID	R_s ($\Omega \cdot cm^2$)	R_f ($\Omega \cdot cm^2$)	$Y_{0\,f}$ ($\mu S \cdot s^n \cdot cm^{-2}$)	n_f	R_{ct} ($k\Omega \cdot cm^2$)	$Y_{0\,dl}$ ($\mu S \cdot s^n \cdot cm^{-2}$)	n_{dl}	χ^2
CEM I pH 12.2	17.7	88.9	226.2	0.788	16.5	3282.1	0.451	0.0005
CEM I pH 12.7	8.1	62.7	203.6	0.796	10.9	1953.9	0.534	0.0006
CEM I pH 13.7	1.8	733.2	771.8	0.680	413.4	443.6	0.903	0.0007

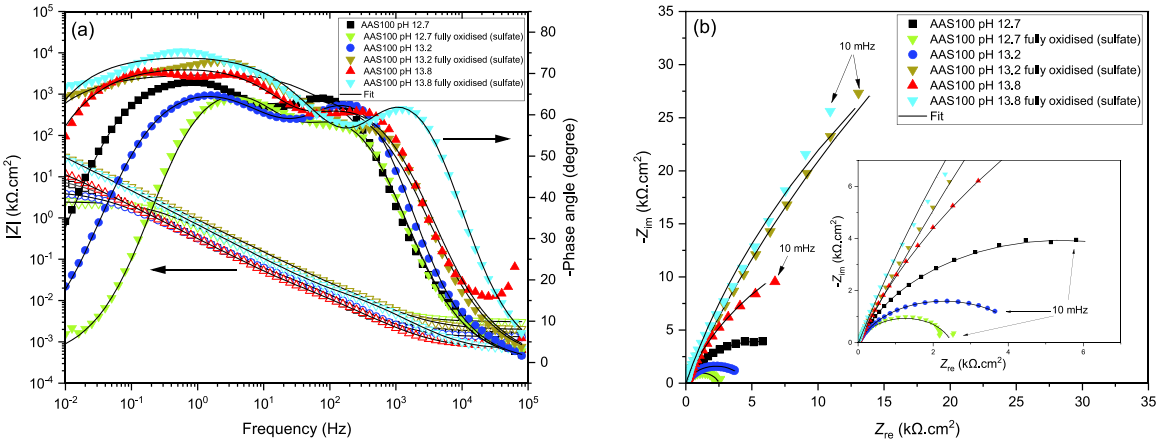


Fig. 10. The EIS responses of steel immersed in chloride-free AAS100 solutions, non-oxidised (anoxic conditions) and fully oxidised (oxic conditions, *i.e.*, oxygen access), at different pH values: (a) Bode plots and (b) Nyquist plots.

Table 8
Fitting parameters obtained from EIS of steel in AAS100 solutions, non-oxidised (anoxic conditions) and fully oxidised (oxic conditions, *i.e.*, oxygen access), at different pH values.

ID	R_s ($\Omega \cdot cm^2$)	R_f ($\Omega \cdot cm^2$)	$Y_{0\,f}$ ($\mu S \cdot s^n \cdot cm^{-2}$)	n_f	R_{ct} ($k\Omega \cdot cm^2$)	$Y_{0\,dl}$ ($\mu S \cdot s^n \cdot cm^{-2}$)	n_{dl}	χ^2
AAS 100 Sulfide pH 12.7 (*anoxic*)	1.5	175.1	487.2	0.806	10.6	252.1	0.796	0.0006
AAS 100 Sulfate pH 12.7 (*oxic*)	3.1	123.0	214.1	0.813	2.4	131.0	0.848	0.0008
AAS 100 Sulfide pH 13.2 (*anoxic*)	1.3	55.8	264.1	0.860	4.5	482.1	0.741	0.0003
AAS 100 Sulfate pH 13.2 (*oxic*)	2.0	292.5	254.6	0.768	243.8	11.6	0.932	0.002
AAS 100 Sulfide pH 13.8 (*anoxic*)	0.7	72.6	564.1	0.781	42.5	160.8	0.864	0.005
AAS 100 Sulfate pH 13.8 (*oxic*)	0.67	57.9	94.9	0.882	152.5	223.6	0.805	0.0006

was unable to assume passivity even in chloride-free solutions, displaying active corrosion from the outset. Consequently, a critical chloride threshold could not be established for these conditions.

The corrosion behaviour of steel in the AAS solutions was dependent on the presence of either sulfide or sulfate, as illustrated in Fig. 12. In the sulfide-containing solutions, steel specimens maintained persistently negative OCP values (–600 to –650 $mV_{Ag/AgCl}$) and low R_p values (5–15 $k\Omega \cdot cm^2$), showing that reduced sulfur species drove the environment into a highly reducing state irrespective of pH or chloride content. Conversely, the electrochemical behaviour of steel in the fully oxidised

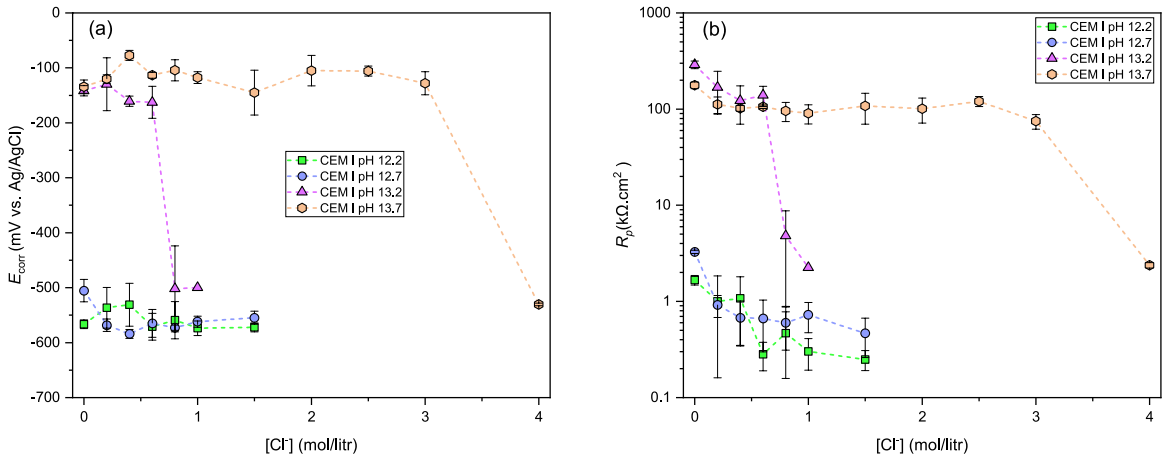


Fig. 11. Evolution of (a) OCP and (b) R_p of steel immersed in synthetic pore solutions of CEM I with varying pH as a function of chloride concentration under oxic conditions (oxygen access).

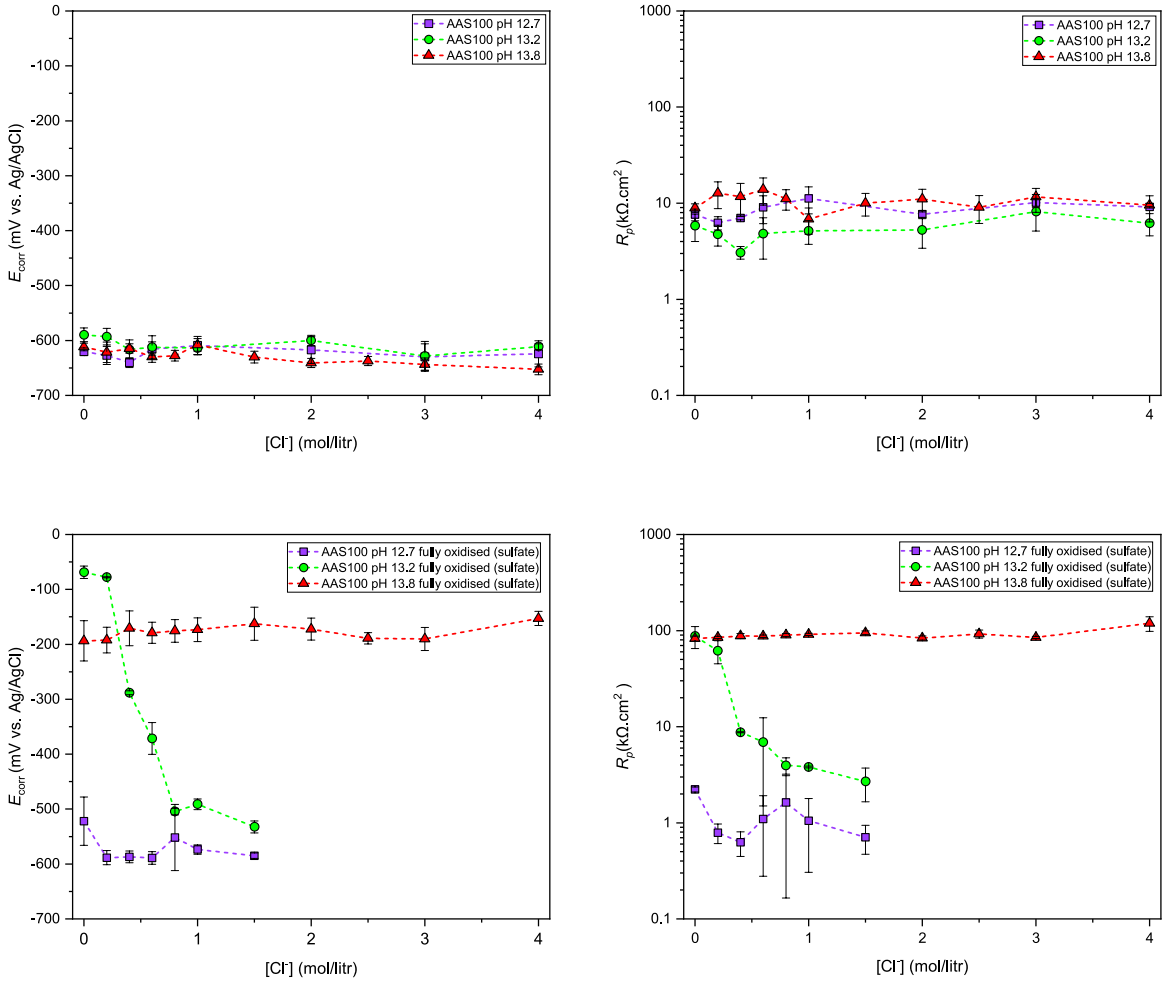


Fig. 12. Evolution of (a) OCP and (b) R_p of steel immersed in synthetic pore solutions of AAS100 with varying pH, and (c) OCP and (d) R_p of steel immersed in fully oxidised synthetic pore solutions of AAS100 with varying pH as a function of chloride concentration under oxic conditions (oxygen access).

(sulfate) AAS100 solution was highly dependent on pH. At pH = 13.8, the steel maintained a stable passive state across the entire chloride range up to 4 M Cl^-, with a noble OCP of approx. –150 $mV_{Ag/AgCl}$ and a high R_p consistently above 80 kΩ·cm^2. For the solution at pH = 13.2, the critical chloride threshold was identified between 0.2 M and 0.4 M Cl^-, where the OCP sharply decreased from its passive state (approx. –70 $mV_{Ag/AgCl}$) to an active state (approx. –290 $mV_{Ag/AgCl}$), accompanied by a corresponding drop of R_p to below 10 kΩ·cm^2. At the lowest pH of 12.7, the steel was unable to passivate even in the absence of chloride, displaying an active corrosion potential of approx. –520 $mV_{Ag/AgCl}$ from the outset.

4. Discussion

4.1. Surface film properties in the presence of sulfides

The present results highlight clear differences between the electrochemical behaviour of steel in sulfide-containing pore solutions and in sulfide-free solutions, such as OPC (CEM I) pore solution. The consistently more negative OCP and lower R_p values observed in the absence of Cl^- in all sulfide-containing pore solutions compared to the CEM I solution indicate a fundamentally different interfacial chemistry. In CEM I solution, the continuous shift of OCP toward more noble values and the increase of R_p over 14 days (Fig. 1) are classic signatures of passivation, *i.e.*, the formation of a dense, protective oxide film on the steel surface [13,43,54]. In contrast, the sulfide-containing systems maintained persistently negative OCPs (−550 to −700 $mV_{Ag/AgCl}$) and low R_p values (3–50 $k\Omega{\cdot}cm^2$), with only minor variation across different sulfide concentrations, and with no visual sign of corrosion (Supplementary Fig. S2), in accord with previous studies on the behaviour of steel in sulfide-containing cement pore solutions [24,28]. This phenomenon can be attributed to the redox characteristics of the sulfide-containing solutions. In such systems, the redox potential of the electrolyte is predominantly controlled by the presence of reduced sulfur species (e.g., HS^-, S_n^{2-}, $S_2O_3^{2-}$, SO_3^{2-}), which create a reducing environment [19,24,55]. Any residual oxygen potentially present in the system will be consumed through the oxidation of these reduced sulfur species. Consequently, when there is no access of oxygen (anoxic conditions), the hydrogen evolution reaction (HER) becomes the dominant cathodic process, further shifting the mixed potential [56] in the negative direction. Additionally, these reduced sulfur species can undergo oxidation at the steel surface, contributing to the overall electrochemical response. Consequently, the measured R_p is not solely indicative of the corrosion resistance of the steel but is instead an "apparent" R_p [57], influenced by the oxidation of the reduced sulfur species rather than just the anodic dissolution of iron [24].

The results obtained from EIS provide evidence supporting this interpretation. R_{ct} quantifies the resistance to electron transfer at the electrode/electrolyte interface, reflecting the kinetics of the electrochemical reactions. Generally, the value of R_{ct} is inversely proportional to the corrosion rate: higher R_{ct} means slower corrosion and *vice versa*. In the present study, the steel in the CEM I solution exhibited a much higher R_{ct} value (479 $k\Omega{\cdot}cm^2$) than steel in the sulfide-containing solutions (35–45 $k\Omega{\cdot}cm^2$) (Table 4). This suggests that the passive film formed in the CEM I environment is highly effective at blocking charge transfer, likely due to a denser, more stable, or less defective film. In contrast, the lower R_{ct} values in the sulfide-containing systems indicate less effective passivation, possibly due to more porous or more defective films, or due to additional electrochemical reactions (e.g., sulfide oxidation) that occur at the steel surface. These reactions may introduce parallel or competing charge transfer processes, potentially lowering the measured R_{ct}.

The effective capacitance of the constant phase element (CPE) (Eqs. 2 and 3), denoted as C_{eff}, further clarifies the nature of the interface. C_{eff} is commonly reported to be expressed as follows when the charge transfer resistance (R_{ct}) is much larger than the solution resistance (R_s) [58–60]:

$$C_{dl(eff)} = {Y_{0dl}}^{1/n_{dl}} . \left(\frac{R_f . R_{ct}}{R_f + R_{ct}}\right)^{(1-n_{dl})/n_{dl}} \quad (2)$$

$$C_{f(eff)} = {Y_{0f}}^{1/n_f} . {R_f}^{(1-n_f)/n_f} \quad (3)$$

where $Y_{0\,f}$ and $Y_{0\,dl}$ denote the CPE admittance parameters for the passive/surface film and the double-layer capacitance, respectively, and n_f and n_{dl} are the corresponding CPE exponents for the passive/surface film and the double-layer capacitance. Table 9 shows the effective capacitance values [C_{dl}(eff) and C_f(eff)] of steel immersed in the synthetic pore solutions of selected systems with differing sulfide concentrations after 14 days of pre-immersion in solutions, calculated based on the fitted parameters of EIS measurement. C_{dl}(eff) and C_f(eff) values represent the system's ability to store charge at the electrical double layer and across the passive/surface film, respectively [61–63]. Higher C_{dl}(eff) values are generally indicative of an increased electrochemically active surface area, greater surface roughness, or a less compact double layer, and higher C_f (eff) values often suggest a thinner, more defective, or porous passive/surface film [61,64,65]. In this study, both C_{dl}(eff) and C_f(eff) values of steel specimens immersed in sulfide-containing synthetic pore solutions were found to be higher than those observed for steel in the CEM I solution. Specifically, C_{dl}(eff) values for steel in sulfide-containing solutions ranged from 80 to 375 $\mu F{\cdot}cm^{-2}$, compared to around 20 $\mu F{\cdot}cm^{-2}$ in the CEM I system. Similarly, C_f (eff) values varied between approx. 110 and 230 $\mu F{\cdot}cm^{-2}$ in the presence of sulfide, whereas the corresponding value for the CEM I solution was about 46 $\mu F{\cdot}cm^{-2}$. These findings suggest that the presence of sulfide leads to increased surface activity and changes in the passive film characteristics, with a potentially more defective or porous passive/-surface film, which is in line with previous studies reporting porous Fe-S complexes formed on the surface of the electrode [23,24]. Direct evidence from XPS analysis in a previous study [24] showed that mild steel exposed to alkaline sulfide solutions within the concentration range used in the present work formed Fe(II)-sulfide and polysulfide species at all investigated sulfide concentrations.

Table 9
The C_{dl} (eff) and C_f (eff) of steel in synthetic pore solutions under anoxic conditions.

ID	C_f (eff) ($\mu F.\ cm^{-2}$)	C_{dl} (eff) ($\mu F.\ cm^{-2}$)
AAS 100	230.25	79.76
AAS 50	109.72	374.05
CEM III	192.88	262.30
CEM III + Act	192.67	244.72
CEM I	46.48	19.72

4.2. Chloride-induced corrosion initiation under anoxic conditions

Steel reinforcement embedded in Portland cement (OPC) concrete is protected against corrosion by formation of a passive film, which is stable until chloride ions reach a threshold concentration, causing localized film breakdown and initiating chloride-induced corrosion and pitting. The critical chloride concentrations required to initiate corrosion in conventional cementitious systems under various experimental conditions are well-established and documented in the literature [5,13, 52,66,67]. In the present study, under anoxic conditions, steel specimens immersed in CEM I solution initially stabilised at approx. −140 $mV_{Ag/AgCl}$ while maintaining a R_p of ~160 $k\Omega{\cdot}cm^2$, indicating a very low corrosion rate in the chloride-free solution. As chloride ions accumulated ([Cl^-] increased), they adsorbed on the passive film, and once their bulk concentration passed a threshold of about 0.6 M, local passive film breakdown occurred, and the OCP and R_p began to decrease (Fig. 5). However, because of the low dissolved oxygen concentration in the solutions, the cathodic reaction is limited (see below), and the anodic dissolution of iron cannot occur at a high rate; thus, even after depassivation, the corrosion rate remained low, as indicated by the moderate decrease in the range 0.6–1.5 M Cl^- instead of a sharp drop of R_p. It should be noted that this moderate decrease instead of an abrupt transition may also result from both the shorter equilibrium period (2 h) and cathodic limitation. In summary, the data indicate that pits nucleated but grew only slowly, and average corrosion rate was low.

In contrast, steel immersed in sulfide-containing pore solution exhibited an inability to form a protective passive layer. In the Fe-H_2O system (Fig. 13**(a)**), protective iron oxides such as Fe_3O_4 and Fe_2O_3 are stable at moderate to high E_h values across a wide pH range, forming dense passive films that inhibit metal dissolution. However, the

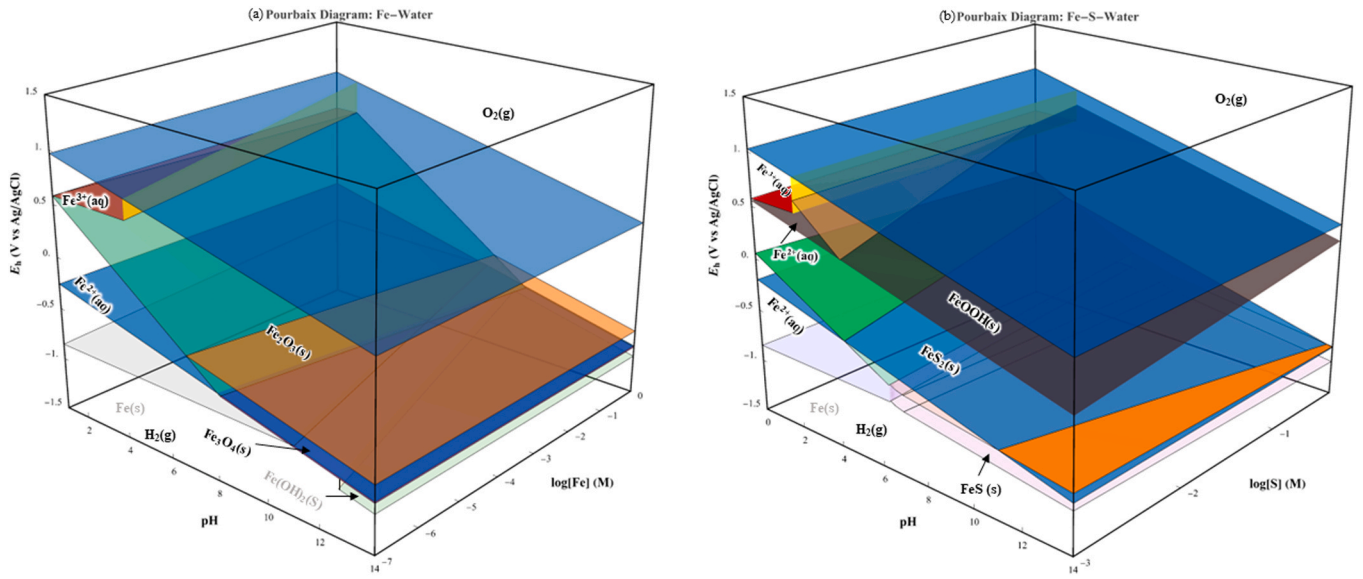


Fig. 13. Three-dimensional Pourbaix diagrams for (a) Fe-H_2O system showing pH-E_h-M with variable iron concentration and (b) Fe-S-H_2O system showing pH-E_h-M with fixed iron concentration (10^{-6} M) and variable sulfur concentration (10^{-3} to 0.5 M).

Pourbaix diagram for the Fe-S-H_2O system (Fig. 13**(b)**) shows that under reducing conditions (low E_h), iron sulfide phases, particularly FeS(s) and FeS_2(s), become thermodynamically stable in the pH range of concrete pore solutions (pH = 12–14). The diagram shows that Fe-S complexes are the thermodynamically stable phases, suppressing oxide formation even at highly alkaline pH. These thermodynamic calculations, together with previous work [24], indicate that the surface layer formed in such solutions is dominated by Fe-S bonds. The Fe-S complexes formed (e.g., with a structure related to the minerals mackinawite and pyrrhotite) are heterogeneous, showing conductive and semiconductive behaviour [26]. The Fe-S layers are thus incapable of acting as an efficient barrier to electron transfer, ionic diffusion (especially aggressive ions like Cl^-) and metal dissolution, and therefore the steel surface remains electrochemically active under anoxic conditions. No abrupt changes of OCP and R_p were observed as chloride was added up to 4 M (Fig. 5), because there was no passive film for the chloride ions to destroy. However, reduced sulfur species are oxygen scavengers, maintaining a reducing and essentially oxygen-free environment; thus, the cathodic reaction of oxygen reduction reaction is suppressed, and the hydrogen evolution reaction becomes the primary cathodic reaction. Compared to oxygen reduction, hydrogen reduction is a significantly slower reaction due to higher activation energy and less favourable kinetics on steel surfaces, especially in high-pH solutions like concrete pore solution [68–70]. Steel is not an efficient hydrogen reduction catalyst, and the use of water (rather than protons) as the hydrogen source in alkaline solution further slows down the reaction. As a result, hydrogen reduction is the dominant cathodic reaction under anoxic conditions, and the overall iron dissolution rate of steel was comparatively low. Finally, it is noted that for solution AAS100, the evolution of OCP and R_p with chloride concentration under anoxic conditions did not depend on pH in the range 12.7–13.8, *i.e.*, pitting was not detected even at the lowest pH of 12.7 and 4 M Cl^- (Fig. 12).

These properties likely have important effects in practical applications. In massive structures made of OPC, such as underwater tunnels, piers, nuclear repositories and wastewater infrastructures, oxygen availability might be limited, and thus conventional corrosion indicators and the classic critical chloride threshold concept may overpredict corrosion risk, as even high chloride concentration cannot cause rapid deterioration without oxygen. When such structures are made with GGBFS-containing cements that release sulfide into solution, the corrosion behaviour of embedded steel reinforcement differs from that in conventional OPC concrete. In concrete made with GGBFS-containing cements, a protective passive layer does not form on the steel surface, regardless of the chloride concentration. Instead, according to the present results, significant corrosion is delayed until all reduced sulfur species, which act as oxygen scavengers, are fully oxidised. This makes conventional corrosion indicators and standards unreliable for assessing corrosion risk in these concretes. Namely, the low redox potential associated with reduced sulfur species can cause the misinterpretation of the results of standard electrochemical methods, assuming the steel to be actively corroding, even when it is not [34]. In cases where cathodic protection is applied based on these incorrect assumptions, overprotection can occur and may promote excessive hydrogen evolution, increasing the risk of hydrogen embrittlement that can lead to cracking and catastrophic structural failure.

It is worth mentioning that the boundaries of the iron sulfide phases stability fields in Fig. 13**(b)** shift only marginally as the total dissolved sulfur concentration is varied over the range 10^{-3} to 0.5 M. This weak dependence indicates that the thermodynamic suppression of protective iron oxides in the pH range of concrete pore solutions is not restricted to systems with high sulfide concentrations, such as AAS100 (350 mM HS^-), but also applies to systems with lower sulfide concentrations.

4.3. Chloride-induced corrosion initiation with access of oxygen

Oxygen availability plays a dual role in steel passivation and chloride-induced corrosion in different cementitious environments. In the CEM I solution, access of oxygen (after the 'pre-passivation' period of 10 days under anoxic conditions) significantly changed the response of the system to increasing chloride concentrations, compared to chloride attack under anoxic conditions. As shown in Fig. 6, under oxic conditions, OCP and R_p remained approximately constant up to a chloride concentration of 3 M. However, when the chloride concentration exceeded this threshold, depassivation occurred, as indicated by a sharp decrease of the OCP to −530 $mV_{Ag/AgCl}$ and a significant reduction of R_p to ~2 $k\Omega{\cdot}cm^2$. This means that a clear c_{crit} was observed, and its value of > 3 M was considerably higher than the concentration range for which a transition has been observed in the anoxic solutions (0.6–1.5 M). The occurrence of a clear chloride threshold can be attributed to the formation a protective passive film on the steel after transfer to the chloride-free solution with oxygen access (facilitated by the high pH of ~13.7 of the solution), its breakdown (*i.e.*, pitting) above the threshold,

and the availability of oxygen for subsequent pit growth. Thus, compared to anoxic conditions, a more protective passive films developed on the surface of steel in the presence of oxygen, and higher chloride concentrations (>3 M) are required to initiate depassivation. However, once the critical chloride threshold was exceeded and the passive layer impaired, the presence of oxygen resulted in a pronounced increase of the corrosion rate, as evidenced by the abrupt decrease of R_p from ~90 kΩ·cm^2 to ~2 kΩ·cm^2.

The CEM III solution was characterized by a lower pH (~12.9), compared to the CEM I solution, and a low sulfide concentration (~10 mM). After transfer to the chloride-free, oxygenated solution, both OCP and R_p decreased considerably at the first chloride increment (0.2 M Cl$^-$), indicating depassivation (Fig. 6). This can be interpreted as indicating that a less protective passive film formed on the surface of the steel, compared to CEM I, due the lower pH of the solution, and possibly the formation of Fe-S complexes in addition to oxides. However, the initial amount of reduced sulfur species in the CEM III solution was insufficient to scavenge all oxygen, as shown by the presence of dissolved oxygen in the solution (Table 5), allowing oxygen reduction to occur as the cathodic reaction in the system.

The response of the steel to increasing chloride concentrations in solutions AAS100, ASS90, AAS75, AAS50, and CEM III + Act was significantly different from the observations for CEM I and CEM III. These solutions, representing alkali-activated GGBFS and hybrid cements, were characterised by high sulfide concentrations and high pH values. In all these cases, the OCP of the steel was low, in the range of approx. −480 $mV_{Ag/AgCl}$ to −680 $mV_{Ag/AgCl}$, and remained at such low values throughout the exposure to oxygen and chloride addition. Similarly, R_p was in the range of approx. 6–15 kΩ·cm^2 and remained essentially constant throughout oxygen exposure and the increase of chloride concentration up to 4 M (Fig. 6). Thus, the behaviour of steel in these solutions did not differ significantly from its behaviour under anoxic conditions. The oxygen concentration in the solutions remained at non-detectable levels throughout the duration of the experiments (Table 5). It can thus be concluded that all oxygen that had dissolved in the solutions was consumed through oxidation of the reduced sulfur species, resulting in the complete depletion of dissolved oxygen in the systems, and therefore continuation of anoxic conditions as regards the corrosion behaviour of the steel in these solutions, limiting the corrosion rates to comparatively low levels. These findings are consistent with previous studies reporting low OCP and R_p values for steel embedded in GGBFS-containing mortars and concretes, without signs of corrosion, for up to more than one year under chloride exposure [27,28]. It can be concluded that in these studies the oxidation of reduced sulfur species to the fully oxidised state was not completed during the experiments, due to slow oxygen diffusion into the mortar/concrete pore solution, and thus the conditions at the steel surface remained essentially anoxic.

4.4. Chloride-induced corrosion initiation in fully oxidised (sulfate) solutions

As indicated above, exposure of GGBFS-containing concrete to air for extended periods of time is likely to lead to oxidation of the reduced sulfur species in the pore solution until they are completely oxidised to sulfate at the steel-concrete interface. The time to reach this condition will strongly depend on the exposure conditions of the concrete, the distance between the outer concrete surface and the steel-concrete interface ('concrete cover thickness'), the pore structure of the concrete, and additional parameters. Although experiments to quantify the effects of these parameters on the rate of advancement of this 'oxidation front' through the concrete are scarce, it may be assumed that the time until it reaches the reinforcing steel will range from months to decades [35–37]. The present experiments in fully oxidised solutions (after 'pre-passivation' in sulfide solutions) are meant to represent this eventual state, no matter when exactly it is reached.

The measured OCP and R_p of the steel specimens in fully oxidised (sulfate) solutions showed a clear difference compared to reducing environments. In the absence of reduced sulfur species, steel specimens that previously failed to form a protective layer were able to form a stable passive layer, which is evidenced by OCP values ranging between −60 $mV_{Ag/AgCl}$ and −200 $mV_{Ag/AgCl}$ and R_p values around 100 kΩ·cm^2 in the chloride-free oxidised solutions (Fig. 7). Steel in AAS100, AAS90, AAS75 and AAS50 solutions maintained their passivity up to 4 M chloride addition due to the high pH (~13.8) value, while the steel in CEM III + Act solution depassivated at a chloride concentration of 2.5 M, as shown by a decrease of OCP and R_p. Steel in the CEM III solution did not form a stable passive film, as evidenced by passive layer break-down at the lowest chloride addition of 0.2 M, with the OCP decreasing from approx. −60 $mV_{Ag/AgCl}$ to −550 $mV_{Ag/AgCl}$ and R_p decreasing from approx. 130 kΩ·cm^2 to 1 kΩ·cm^2. This can be assigned to the fact that the pH of the oxidised CEM III solution was 12.9., *i.e.*, considerably lower than the pH of the other solutions (pH = 13.6–13.8). The effect of solution CEM III is thus in line with the literature reporting a direct correlation between pH and the critical chloride concentration for depassivation [5,21,52].

The EIS results (Fig. 8 and Table 6) provide detailed evidence of passive film quality and chloride resistance across the tested systems. In chloride-free conditions, all systems demonstrated effective passive film formation, with high charge transfer resistance (R_{ct} = 150–425 kΩ·cm^2), impedance values of 20–30 kΩ·cm^2 at low frequencies, and phase angle maxima of approx. 75° for CEM I and 70° for AAS systems, indicating near-ideal capacitive behaviour characteristic of compact, homogeneous passive films. Upon addition of 4 M chloride, steel in CEM I and CEM III solutions showed severe passive film degradation, with R_{ct} decreasing to 1.6 and 1.8 kΩ·cm^2, impedance decreasing to ~2 kΩ·cm^2, and significantly reduced phase angles, indicating chloride-induced breakdown and active corrosion. In contrast, AAS100 and AAS50 systems maintained high impedance (20–30 kΩ·cm^2) and phase angles (~75°) even at 4 M chloride concentration, demonstrating superior chloride resistance. This behaviour indicates that after complete oxidation of reduced sulfur species to sulfate, steel in AAS systems retains effective protection against chloride-induced corrosion, likely due to their higher pH and unique pore solution chemistry.

The relationship between critical chloride threshold and pH was further confirmed in the present study by the experiments for fully oxidised solutions CEM I and AAS100 with varied pH values (Figs. 11 and 12). At the highest pH values, the steel exhibited high chloride tolerance with no depassivation observed up to 4 M Cl$^-$ (AAS100, pH = 13.8), or a threshold between 3 and 4 M Cl$^-$ (CEM I, pH = 13.7), consistent with the high OH$^-$ concentration in these solutions promoting stable passive film formation. The OCP in the range of −70 to −200 $mV_{Ag/AgCl}$ and high R_p (> 90 kΩ·cm^2) indicate the formation of a stable passive layer, mainly composed of iron oxide phases that are thermodynamically stable under these highly alkaline conditions. The reduction at pH = 13.2 of the chloride threshold to 0.2–0.4 M Cl$^-$ for AAS100 and to 0.6–0.8 M Cl$^-$ for CEM I demonstrates the critical nature of the [Cl$^-$]/[OH$^-$] ratio in determining depassivation susceptibility. This behaviour follows point defect model predictions [71], where higher pH suppresses barrier layer dissolution and stabilises film defect structure, while reduced alkalinity accelerates dissolution processes that weaken passivity. The inability of the steel to maintain passivity at pH values of 12.7 and 12.2, even in chloride-free solutions, indicates that a minimum hydroxyl ion concentration is required for passive film stability. This threshold behaviour reflects the transition from a protective oxide/-hydroxide film to an unstable, defect-rich surface layer that cannot provide adequate corrosion protection.

The EIS results provide additional understanding of the basis for the observed pH effects. In CEM I systems, the systematic increase in solution resistance (R_s) with decreasing pH (1.8–17.7 Ω·cm^2) (Table 7) reflects changes of the ionic composition and conductivity as the system moves away from the highly alkaline solution dominated by OH$^-$ ions. More significantly, the abrupt reduction in passive film resistance (R_f)

from 733.2 Ω·cm^2 at pH = 13.7 to 88.9 Ω·cm^2 at pH = 12.2 demonstrates the deterioration of film quality with decreasing alkalinity. The charge-transfer resistance (R_{ct}) values provide the most direct measure of corrosion susceptibility, with the high value of 413.4 kΩ·cm^2 at pH = 13.7 confirming excellent passivation. The abrupt drop to approx. 10–16 kΩ·cm^2 at lower pH values indicates a transition to active corrosion behaviour.

Finally, to further demonstrate the influence of pH on the formation of passive film, the thickness (δ) of the passive film can be estimated using the following Eq. (4). [59]

$$\delta = \frac{(\varepsilon\varepsilon_0)^{n_f}}{Y_{0f}(\rho_\delta)^{1-n_f}} \quad (4)$$

where ε is the relative dielectric constant (taken as $\varepsilon = 12$, the dielectric constant of Fe_2O_3), ε_0 is the vacuum permittivity (8.854×10^{-14} F/cm) and ρ_δ is the oxide resistivity ($\rho_\delta = 450$ Ω·cm^2) [72]. Table 10 shows the effective capacitance values and the estimated passive film thickness of steel specimens in CEM I solutions with varying pH. The effective capacitance values suggest that higher pH conditions favour more homogeneous and protective passive films, less electrochemically active surface area and thicker and less defective passive films. Accordingly, the estimated film thickness at high pH is approx. 13 nm, while at low pH it is around 4 nm. The Bode plots support these conclusions, with the high impedance values (approx. 30 kΩ·cm^2) and phase angle maximum at low frequency (approx. 77°) at pH = 13.7 (Fig. 9**(a)**) indicating near-ideal capacitive behaviour characteristics of a dense, uniform passive film. The progressive decrease in phase angle maxima at low frequency with reducing pH reflects increasing heterogeneity and reduced protective capacity of the surface films.

In the fully oxidised solutions, the sulfate concentration varies between the solutions (Table 2). If sulfate acted synergistically with chloride, chloride resistance would be expected to decrease with increasing sulfate concentration. However, the observation is inconsistent with this, since steel in AAS100 and AAS50 both remained passive up to 4 M Cl$^-$, whereas steel in CEM III + Act depassivated at 2.5 M Cl$^-$. This is consistent with the mechanism proposed by Liu et al. [73], in which sulfate, adsorbing more strongly on the Fe(100) surface than chloride, displaces it from adsorption sites while acting as the weaker catalyst during propagation, so that mixed chloride–sulfate systems may present a corrosion risk between those of the single aggressive anions.

4.5. Relative contributions of reduced sulfur species, oxygen and pH

The results show that sulfide concentration, oxygen availability and pH affect corrosion in a clear order of importance rather than equally. Reduced sulfur species are the main factor because they consume oxygen and maintain reducing conditions in which non-protective iron sulfide complexes, rather than protective iron oxides, are stable. As a result, no passive film forms and chloride additions do not initiate corrosion. Oxygen is the second factor and becomes important only after the reduced sulfur species have been completely oxidised to sulfate. At this stage, steel can passivate and pH becomes the main factor controlling corrosion behaviour. Higher pH promotes stable passivation and higher chloride resistance and on the other hand lower pH leads to depassivation or prevents passivation. Therefore, sulfide determines the corrosion regime, oxygen controls the transition to passivity, and pH controls chloride resistance only after reduced sulfur species have been fully oxidised. Table 11 summarises these corrosion regimes.

Table 10
The C_{dl}(eff), C_f(eff) and calculated thickness (δ) of the surface film for steel immersed in CEM I solutions at different pH values.

ID	C_f (eff) (μF. cm^{-2})	C_{dl} (eff) (μF. cm^{-2})	δ (nm)
CEM I pH 12.2	79.1	727.8	4.4
CEM I pH 12.7	66.6	311.0	4.2
CEM I pH 13.7	20.2	393.1	13.2

4.6. Transferability of results to concrete

In this study, the experiments were conducted in synthetic pore solutions with freely exposed steel to isolate the effects of sulfide concentration, oxygen availability, and pH. However, key parameters of real concrete, such as pore structure, moisture dynamics, chloride binding, and the heterogeneous steel/concrete interface [9,54,74–76], are excluded in this study. Consequently, the reported chloride concentrations serve as comparative metrics for relative chloride tolerance rather than direct engineering design values. However, the sustained reducing conditions observed during air exposure are expected to be transferable to real structures. Given that oxygen ingress in concrete is severely limited by diffusion through a dense, saturated cover, the reducing regime reported here provides a conservative lower limit.

5. Conclusions

This study investigated the electrochemical behaviour of steel in synthetic pore solutions representing CEM I and sulfide-containing cements, revealing fundamentally different corrosion protection mechanisms, depending on the presence of reduced sulfur species, oxygen availability, and pH. Under anoxic conditions, steel in CEM I exhibited classical passivation behaviour with comparatively high OCP (approx. −150 $mV_{Ag/AgCl}$), high R_p (approx. 160 kΩ·cm^2), and clear critical chloride thresholds (0.6–0.8 M Cl$^-$). In contrast, all sulfide-containing solutions showed negative OCPs (−500 to −800 $mV_{Ag/AgCl}$), lower R_p (20–50 kΩ·cm^2). A clear c_{crit} was not observed for steel in solutions with high concentrations of reduced sulfur species, because reduced sulfur species effectively prevented stable passive film formation and acted as oxygen scavengers, maintaining anoxic conditions at the steel surface even under atmospheric exposure until the reduced sulfur species are eventually fully oxidised. Following complete sulfur species oxidation to sulfate, the steel in those solutions showed better chloride-induced corrosion resistance compared to CEM I, with passive film formation ($R_p \approx 100$ kΩ·cm^2, impedance 20–30 kΩ·cm^2), attributed to higher alkalinity and unique pore solution chemistry. pH variation studies confirmed that in sulfide-containing solutions, reduced sulfur chemistry completely dominated over pH effects, while in fully oxidised systems,

Table 11
Controlling factors and corrosion behaviour of steel in the three regimes identified in this work.

	Regime I: reducing, oxygen excluded	Regime II: reducing, oxygen admitted but scavenged	Regime III: fully oxidised
Reduced sulfur species at steel surface	Present	Present	Absent
Dissolved oxygen at steel surface	Absent	Absent (consumed)	Present
Dominant cathodic reaction	Hydrogen evolution	Hydrogen evolution	Oxygen reduction
Surface layer	non-protective	non-protective	passive film/ protective
Influence of pH	No systematic dependence over pH 12.7–13.8[a]	No systematic dependence over pH 12.7–13.8[a]	Dominant control
Chloride threshold concept	Not applicable	Not applicable	Applicable, strongly pH dependent

[a] pH was varied systematically only in the AAS100 sulfide-containing series (Fig. 12**(a) and (b)**).

conventional pH-dependent chloride thresholds emerged.

The detrimental effect of reduced sulfur species on passivation of steel is transient and ends once the oxidation front reaches the reinforcement and fully oxidise the reduced sulfur species. However, because its duration is controlled by oxygen diffusion, oxidation kinetics and the initial reduced sulfur species concentration, it may persist for decades in dense, high-GGBFS concretes [35–37]. Corrosion initiation is therefore governed by two independently advancing fronts, the chloride front and the oxidation front, whereas current service life models consider only the chloride front.

These findings have critical implications for the design and service life prediction of reinforced concrete structures incorporating GGBFS. Current models based on $[Cl^-]/[OH^-]$ ratios and passive film breakdown are inadequate for high-GGBFS systems, where steel exists in a state with corrosion rates controlled by oxygen diffusion and reduced sulfur species oxidation rather than only chloride-induced depassivation. Future research should prioritize quantifying sulfide oxidation kinetics in concrete pore solutions under various exposure conditions and validating these findings in mortar and concrete specimens, combined with systematic investigations of the steel-concrete interface. Advanced surface characterisation techniques are needed to identify the chemical composition and structure of surface films formed under different conditions. Understanding whether surface film consists of iron sulfides, modified oxides, or mixed-phase layers compared to conventional passive films is fundamental for developing mechanistic corrosion protection models and translating these findings into reliable design guidance for GGBFS-containing reinforced concrete structures. Also, future research should prioritise the quantification of sulfide oxidation kinetics in concrete pore solutions under realistic exposure conditions, and the validation of the present findings in mortar and concrete specimens, where the effects mentioned in Section 4.6 act together with the pore solution chemistry.

CRediT authorship contribution statement

Ali Nikoonasab: Writing – review & editing, Writing – original draft, Visualization, Methodology, Investigation, Formal analysis, Data curation. **Thoralf Müller:** Writing – review & editing, Methodology. **Michael Raupach:** Writing – review & editing, Supervision, Funding acquisition, Conceptualization. **Gregor J.G. Gluth:** Writing – review & editing, Supervision, Methodology, Funding acquisition, Conceptualization.

Declaration of Competing Interest

The authors declare that they have no known competing financial interests or personal relationships that could have appeared to influence the work reported in this paper.

Acknowledgements

The work leading to the present results was funded by the Deutsche Forschungsgemeinschaft (DFG, German Research Foundation) – Project number 458297195, which is gratefully acknowledged.

Appendix A. Supporting information

Supplementary data associated with this article can be found in the online version at doi:10.1016/j.conbuildmat.2026.147963.

Data availability

Data will be made available on request.

References

[1] U.M. Angst, Challenges and opportunities in corrosion of steel in concrete, Mater. Struct. 51 (2018) 4, https://doi.org/10.1617/s11527-017-1131-6.
[2] C.L. Page, K.W.J. Treadaway, Aspects of the electrochemistry of steel in concrete, Nature 297 (1982) 109–115, https://doi.org/10.1038/297109a0.
[3] G.H. Koch, M.P.H. Brongers, N.G. Thompson, Y.P. Virmani, J.H. Payer JH, Corrosion cost and preventive strategies in the United States, Federal Highway Administration, McLean, 2002. https://rosap.ntl.bts.gov/view/dot/40697.
[4] D. Dwivedi, K. Lepková, T. Becker, Carbon steel corrosion: a review of key surface properties and characterization methods, RSC Adv. 7 (2017) 4580–4610, https://doi.org/10.1039/C6RA25094G.
[5] V.K. Gouda, W.Y. Halaka, Corrosion and corrosion inhibition of reinforcing steel: II. Embedded in concrete, Br. Corros. J. 5 (1970) 204–208, https://doi.org/10.1179/000705970798324478.
[6] J.L. Provis, Alkali-activated materials, Cem. Concr. Res. 114 (2018) 40–48, https://doi.org/10.1016/j.cemconres.2017.02.009.
[7] J. Osio-Norgaard, J.P. Gevaudan, W.V. Srubar, A review of chloride transport in alkali-activated cement paste, mortar, and concrete, Constr. Build. Mater. 186 (2018) 191–206, https://doi.org/10.1016/j.conbuildmat.2018.07.119.
[8] A. Runci, J. Provis, M. Serdar, Microstructure as a key parameter for understanding chloride ingress in alkali-activated mortars, Cem. Concr. Compos. 134 (2022) 104818, https://doi.org/10.1016/j.cemconcomp.2022.104818.
[9] O. Kayali, M.S.H. Khan, M.S. Ahmed, The role of hydrotalcite in chloride binding and corrosion protection in concretes with ground granulated blast furnace slag, Cem. Concr. Compos. 34 (2012) 936–945, https://doi.org/10.1016/j.cemconcomp.2012.04.009.
[10] X. Ke, S.A. Bernal, J.L. Provis, Uptake of chloride and carbonate by Mg-Al and Ca-Al layered double hydroxides in simulated pore solutions of alkali-activated slag cement, Cem. Concr. Res. 100 (2017) 1–13, https://doi.org/10.1016/j.cemconres.2017.05.015.
[11] G.J.G. Gluth, S. Mundra, R. Henning, Chloride binding by layered double hydroxides (LDH/AFm phases) and alkali-activated slag pastes: an experimental study by RILEM TC 283-CAM, Mater. Struct. 57 (2024) 72, https://doi.org/10.1617/s11527-024-02311-3.
[12] G. Gu, T. Ma, R. Qian, H. Ye, L. Wan-Wendner, C. Fu, Evolution of chloride binding and mechanical behavior in metakaolin-based geopolymer: role of MgO-induced phase changes, Constr. Build. Mater. 478 (2025) 141424, https://doi.org/10.1016/j.conbuildmat.2025.141424.
[13] U. Angst, B. Elsener, C.K. Larsen, Ø. Vennesland, Critical chloride content in reinforced concrete – a review, Cem. Concr. Res. 39 (2009) 1122–1138, https://doi.org/10.1016/j.cemconres.2009.08.006.
[14] I.G. Ogunsanya, C.M. Hansson, Detection of the critical chloride threshold of carbon steel rebar in synthetic concrete pore solutions, RILEM Tech. Lett. 3 (2019) 75–83, https://doi.org/10.21809/rilemtechlett.2018.70.
[15] S.M. Abd El Haleem, S. Abd El Wanees, A. Bahgat, Environmental factors affecting the corrosion behaviour of reinforcing steel. V. Role of chloride and sulphate ions in the corrosion of reinforcing steel in saturated $Ca(OH)_2$ solutions, Corros. Sci. 75 (2013) 1–15, https://doi.org/10.1016/j.corsci.2013.04.049.
[16] A. Gruskovnjak, B. Lothenbach, L. Holzer, R. Figi, F. Winnefeld, Hydration of alkali-activated slag: comparison with ordinary Portland cement, Adv. Cem. Res. 18 (2006) 119–128, https://doi.org/10.1680/adcr.2006.18.3.119.
[17] A. Scott, M.G. Alexander, Effect of supplementary cementitious materials (binder type) on the pore solution chemistry and the corrosion of steel in alkaline environments, Cem. Concr. Res. 89 (2016) 45–55, https://doi.org/10.1016/j.cemconres.2016.08.007.
[18] A. Vollpracht, B. Lothenbach, R. Snellings, J. Haufe, The pore solution of blended cements: a review, Mater. Struct. 49 (2016) 3341–3367, https://doi.org/10.1617/s11527-015-0724-1.
[19] A. Nikoonasab, M. Licht, L. Weiler, R. Achenbach, M. Raupach, G.J.G. Gluth, Pore solution compositions and redox potentials of ground granulated blast furnace slag-containing cement pastes, Adv. Cem. Res. 38 (2026) 238–249, https://doi.org/10.1680/jadcr.25.00041.
[20] P. Ghods, O.B. Isgor, G. McRae, T. Miller, The effect of concrete pore solution composition on the quality of passive oxide films on black steel reinforcement, Cem. Concr. Compos. 31 (2009) 2–11, https://doi.org/10.1016/j.cemconcomp.2008.10.003.
[21] V.K. Gouda, Corrosion and corrosion inhibition of reinforcing steel. I. Immersed in alkaline solutions, Br. Corros. J. 5 (1970) 198–203, https://doi.org/10.1179/000705970798324450.
[22] A. Poursaee, C.M. Hansson, Reinforcing steel passivation in mortar and pore solution, Cem. Concr. Res. 37 (2007) 1127–1133, https://doi.org/10.1016/j.cemconres.2007.04.005.
[23] X. Guan, B.C. Enalls, D.R. Clarke, P. Girguis, Iron sulfide formation on iron substrates by electrochemical reaction in anoxic conditions, Cryst. Growth Des. 17 (2017) 6332–6340, https://doi.org/10.1021/acs.cgd.7b01013.
[24] S. Mundra, J.L. Provis, Mechanisms of passivation and chloride-induced corrosion of mild steel in sulfide-containing alkaline solutions, J. Mater. Sci. 56 (2021) 14783–14802, https://doi.org/10.1007/s10853-021-06237-x.
[25] B.D. Cahan, C.T. Chen, Closure to "Discussion of 'The nature of the passive film on iron. II. A-C impedance studies' [B. Cahan and C. T. Chen (pp. 474–480, Vol. 129, No. 3)], J. Electrochem. Soc. 129 (1982) 2873, https://doi.org/10.1149/1.2123704.
[26] D. Rickard, G.W. Luther, III, Chemistry of iron sulfides, Chem. Rev. 107 (2007) 514–562, https://doi.org/10.1021/cr0503658.

[27] V. Bouteiller, C. Cremona, V. Baroghel-Bouny, A. Maloula, Corrosion initiation of reinforced concretes based on Portland or GGBS cements: chloride contents and electrochemical characterizations versus time, Cem. Concr. Res. 42 (2012) 1456–1467, https://doi.org/10.1016/j.cemconres.2012.07.004.
[28] M. Criado, J.L. Provis, Alkali activated slag mortars provide high resistance to chloride-induced corrosion of steel, Front. Mater. 5 (2018) 34, https://doi.org/10.3389/fmats.2018.00034.
[29] D.E. Macphee, H.T. Cao, Theoretical description of impact of blast furnace slag (BFS) on steel passivation in concrete, Mag. Concr. Res. 45 (1993) 63–69, https://doi.org/10.1680/macr.1993.45.162.63.
[30] J.-S. Lee, Y. Kitagawa, T. Nakanishi, Y. Hasegawa, K. Fushimi, Passivation behavior of type-316L stainless steel in the presence of hydrogen sulfide ions generated from a local anion generating system, Electrochim. Acta 220 (2016) 304–311, https://doi.org/10.1016/j.electacta.2016.10.124.
[31] D.W. Shoesmith, M.G. Bailey, B. Ikeda, Electrochemical formation of mackinawite in alkaline sulphide solutions, Electrochim. Acta 23 (1978) 1329–1339, https://doi.org/10.1016/0013-4686(78)80013-9.
[32] D.W. Shoesmith, P. Taylor, M.G. Bailey, B. Ikeda, Electrochemical behaviour of iron in alkaline sulphide solutions, Electrochim. Acta 23 (1978) 903–916, https://doi.org/10.1016/0013-4686(78)87014-5.
[33] X. Xu, X. Hu, A. Khaskhoussi, C. Shi, Passivation and depassivation of reinforcement steel in alkali-activated materials—a review, Cem. Concr. Compos. 154 (2024) 105802, https://doi.org/10.1016/j.cemconcomp.2024.105802.
[34] S. Mundra, G. Samson, G. Masi, R. Achenbach, D.M. Bastidas, S.A. Bernal, M. C. Bignozzi, M. Criado, M. Cyr, N. Gartner, S. von Greve-Dierfeld, A. Legat, A. Nikoonasab, J.L. Provis, M. Raupach, G.J.G. Gluth, Application of electrochemical methods for studying steel corrosion in alkali-activated materials, Mater. Corros. 74 (2023) 988–1008, https://doi.org/10.1002/maco.202313743.
[35] P. Azar, G. Samson, C. Patapy, F. Cussigh, L. Frouin, R. Idir, M. Cyr, Durability of sodium carbonate alkali-activated slag concrete assessed by a performance-based approach, Constr. Build. Mater. 423 (2024) 135873, https://doi.org/10.1016/j.conbuildmat.2024.135873.
[36] P. Azar, G. Samson, C. Patapy, F. Cussigh, L. Frouin, M. Cyr, Carbonation-induced corrosion of steel in sodium carbonate alkali-activated slag, Mater. Struct. 58 (2025) 252, https://doi.org/10.1617/s11527-025-02696-9.
[37] L.U.D. Tambara Jr, A. Nikoonasab, M. Radtke, A. Guilherme Buzanich, G.J. G. Gluth, Determination of the oxidation depths of ground granulated blast furnace slag-containing cement pastes using Mn K-edge X-ray absorption near-edge structure spectroscopy, J. Am. Ceram. Soc. 109 (2026) e70445, https://doi.org/10.1111/jace.70445.
[38] D.E. Macphee, H.T. Cao, R.B. Polder, R.F.M. Bakker, Discussion: Theoretical description of impact of blastfurnace slag (BFS) on steel passivation in concrete, Mag. Concr. Res. 46 (1994) 151–154, https://doi.org/10.1680/macr.1994.46.167.151.
[39] A. Palomo, P. Monteiro, P. Martauz, V. Bílek, A. Fernandez-Jimenez, Hybrid binders: a journey from the past to a sustainable future (*opus caementitium futurum*), Cem. Concr. Res. 124 (2019) 105829, https://doi.org/10.1016/j.cemconres.2019.105829.
[40] G.J.G. Gluth, S. Garel, Calorimetry study of the influence of Portland cement content, slag/fly ash ratio, and activator type on the early hydration of hybrid cements, in: I.B. Valente, A. Ventura Gouveia, S.S. Dias (Eds.), Proceedings of the 3rd RILEM Spring Convention and Conference (RSCC 2020) – Volume 2: New Materials and Structures for Ultra-durability, RILEM Bookseries, 33, Springer, Cham, 2021, pp. 217–226, https://doi.org/10.1007/978-3-030-76551-4_20.
[41] J.M. Etcheverry, Z. Yue, S. Krishnan, Y.A. Villagran-Zaccardi, P. Van den Heede, Y. Dhandapani, S.A. Bernal, N. De Belie, Phase evolution of hybrid alkali sulfate-activated ground-granulated blast furnace slag cements, ACS Sustain. Chem. Eng. 11 (2023) 17519–17531, https://doi.org/10.1021/acssuschemeng.3c05937.
[42] A. Nikoonasab, T. Müller, G.J.G. Gluth, Study of steel behavior in synthetic pore solutions of GGBFS-containing cements using EIS, Int. Workshop Impedance Spectrosc. (IWIS) 2024 (2024) 44–48, https://doi.org/10.1109/IWIS63047.2024.10847235.
[43] U.M. Angst, B. Elsener, C.K. Larsen, Ø. Vennesland, Chloride induced reinforcement corrosion: electrochemical monitoring of initiation stage and chloride threshold values, Corros. Sci. 53 (2011) 1451–1464, https://doi.org/10.1016/j.corsci.2011.01.025.
[44] A.J. Bard, R. Parsons, J. Jordan (Eds.), Standard Potentials in Aqueous Solutions, IUPAC/Marcel Dekker, New York, 1985.
[45] E. Garcia, J. Torres, N. Rebolledo, R. Arrabal, J. Sanchez, Corrosion of steel rebars in anoxic environments. Part I: Electrochemical measurements, Materials 14 (2021) 2491, https://doi.org/10.3390/ma14102491.
[46] P. Lu, S. Sharifi-Asl, B. Kursten, D.D. Macdonald, The irreversibility of the passive state of carbon steel in the alkaline concrete pore solution under simulated anoxic conditions, J. Electrochem. Soc. 162 (2015) C572–C581, https://doi.org/10.1149/2.0731510jes.
[47] M. Sánchez, J. Gregori, M.C. Alonso, J.J. García-Jareño, F. Vicente, Anodic growth of passive layers on steel rebars in an alkaline medium simulating the concrete pores, Electrochim. Acta 52 (2006) 47–53, https://doi.org/10.1016/j.electacta.2006.03.071.
[48] M. Sánchez, J. Gregori, C. Alonso, J.J. García-Jareño, H. Takenouti, F. Vicente, Electrochemical impedance spectroscopy for studying passive layers on steel rebars immersed in alkaline solutions simulating concrete pores, Electrochim. Acta 52 (2007) 7634–7641, https://doi.org/10.1016/j.electacta.2007.02.012.
[49] J. Shi, J. Ming, W. Sun, Electrochemical performance of reinforcing steel in alkali-activated slag extract in the presence of chlorides, Corros. Sci. 133 (2018) 288–299, https://doi.org/10.1016/j.corsci.2018.01.043.
[50] C.-Q. Ye, R.-G. Hu, S.-G. Dong, X.-J. Zhang, R.-Q. Hou, R.-G. Du, C.-J. Lin, J.-S. Pan, EIS analysis on chloride-induced corrosion behavior of reinforcement steel in simulated carbonated concrete pore solutions, J. Electroanal. Chem. 688 (2013) 275–281, https://doi.org/10.1016/j.jelechem.2012.09.012.
[51] M. Urquidi-Macdonald, A. Almarzooqi, B. Kursten, D.D. Macdonald, On the stability of the passive film on carbon steel as indicated by electrochemical impedance spectroscopy, ECS Trans. 50 (2013) 283–302, https://doi.org/10.1149/05031.0283ecst.
[52] D.A. Hausmann, Steel corrosion in concrete: How does it occur? Mater. Prot. 6 (11) (1967) 19–23.
[53] M.F. Montemor, A.M.P. Simões, M.G.S. Ferreira, Chloride-induced corrosion on reinforcing steel: from the fundamentals to the monitoring techniques, Cem. Concr. Compos. 25 (2003) 491–502, https://doi.org/10.1016/S0958-9465(02)00089-6.
[54] F. Hunkeler, Corrosion in reinforced concrete: processes and mechanisms, in: H. Böhni (Ed.), Corrosion in Reinforced Concrete Structures, Woodhead, Cambridge, 2005, pp. 1–45, https://doi.org/10.1533/9781845690434.1.
[55] M.J. Angus, F.P. Glasser, The chemical environment in cement matrices, in: L. O. Werme (Ed.), Scientific Basis for Nuclear Waste Management IX, Materials Research Society Symposium Proceedings 50, Materials Research Society, Pittsburgh, 1985, pp. 547–556, https://doi.org/10.1557/PROC-50-547.
[56] N. Perez. Electrochemistry and Corrosion Science, 2nd ed., Springer, 2016.
[57] M.E. Orazem. Underground Pipeline Corrosion, Woodhead, 2014.
[58] G.J. Brug, A.L.G. van den Eeden, M. Sluyters-Rehbach, J.H. Sluyters, The analysis of electrode impedances complicated by the presence of a constant phase element, J. Electroanal. Chem. Interfacial Electrochem. 176 (1984) 275–295, https://doi.org/10.1016/S0022-0728(84)80324-1.
[59] B. Hirschorn, M.E. Orazem, B. Tribollet, V. Vivier, I. Frateur, M. Musiani, Determination of effective capacitance and film thickness from constant-phase-element parameters, Electrochim. Acta 55 (2010) 6218–6227, https://doi.org/10.1016/j.electacta.2009.10.065.
[60] N. You, J. Shi, Y. Zhang, Electrochemical performance of low-alloy steel and low-carbon steel immersed in the simulated pore solutions of alkali-activated slag/steel slag pastes in the presence of chlorides, Corros. Sci. 205 (2022) 110438, https://doi.org/10.1016/j.corsci.2022.110438.
[61] E.F. Douglass Jr, P.F. Driscoll, D. Liu, N.A. Burnham, C.R. Lambert, W. G. McGimpsey, Effect of electrode roughness on the capacitive behavior of self-assembled monolayers, Anal. Chem. 80 (2008) 7670–7677, https://doi.org/10.1021/ac800521z.
[62] O. Gharbi, M.T.T. Tran, B. Tribollet, M. Turmine, V. Vivier, Revisiting cyclic voltammetry and electrochemical impedance spectroscopy analysis for capacitance measurements, Electrochim. Acta 343 (2020) 136109, https://doi.org/10.1016/j.electacta.2020.136109.
[63] M. Schalenbach, V. Selmert, A. Kretzschmar, L. Raijmakers, Y.E. Durmus, H. Tempel, R.-A. Eichel, How microstructures, oxide layers, and charge transfer reactions influence double layer capacitances. Part 1: impedance spectroscopy and cyclic voltammetry to estimate electrochemically active surface areas (ECSAs), Phys. Chem. Chem. Phys. 26 (2024) 14288–14304, https://doi.org/10.1039/D3CP04743A.
[64] S.P. Harrington, T.M. Devine, Relation between the semiconducting properties of a passive film and reduction reaction rates, J. Electrochem. Soc. 156 (2009) C154–C159, https://doi.org/10.1149/1.3077576.
[65] M.E. Orazem, I. Frateur, B. Tribollet, V. Vivier, S. Marcelin, N. Pébère, A.L. Bunge, E.A. White, D.P. Riemer, M. Musiani, Dielectric properties of materials showing constant-phase-element (CPE) impedance response, J. Electrochem. Soc. 160 (2013) C215–C225, https://doi.org/10.1149/2.033306jes.
[66] C. Andrade, J.A. González, Quantitative measurements of corrosion rate of reinforcing steels embedded in concrete using polarization resistance measurements, Werkst. Korros. 29 (1978) 515–519, https://doi.org/10.1002/maco.19780290804.
[67] S. Goñi, C. Andrade, Synthetic concrete pore solution chemistry and rebar corrosion rate in the presence of chlorides, Cem. Concr. Res. 20 (1990) 525–539, https://doi.org/10.1016/0008-8846(90)90097-H.
[68] I. Ledezma-Yanez, W.D.Z. Wallace, P. Sebastián-Pascual, V. Climent, J.M. Feliu, M. T.M. Koper, Interfacial water reorganization as a pH-dependent descriptor of the hydrogen evolution rate on platinum electrodes, Nat. Energy 2 (2017) 17031, https://doi.org/10.1038/nenergy.2017.31.
[69] W. Sheng, H.A. Gasteiger, Y. Shao-Horn, Hydrogen oxidation and evolution reaction kinetics on platinum: acid vs alkaline electrolytes, J. Electrochem. Soc. 157 (2010) B1529–B1536, https://doi.org/10.1149/1.3483106.
[70] Y. Zheng, Y. Jiao, A. Vasileff, S.-Z. Qiao, The hydrogen evolution reaction in alkaline solution: from theory, single crystal models, to practical electrocatalysts, Angew. Chem. Int. Ed. 57 (2018) 7568–7579, https://doi.org/10.1002/anie.201710556.
[71] D.D. Macdonald, The history of the Point Defect Model for the passive state: a brief review of film growth aspects, Electrochim. Acta 56 (2011) 1761–1772, https://doi.org/10.1016/j.electacta.2010.11.005.
[72] CRC Handbook of Chemistry and Physics 87th ed. 2007 CRC Press.
[73] G. Liu, J. Li, Y. Zhang, Corrosion of carbon steels subjected to chloride and sulfate in simulated concrete pore solutions with different pH, Const. Build. Mater. 440 (2024) 137445, https://doi.org/10.1016/j.conbuildmat.2024.137445.
[74] U.M. Angst, M.R. Geiker, A. Michel, C. Gehlen, H. Wong, O.B. Isgor, B. Elsener, C. M. Hansson, R. François, K. Hornbostel, R. Polder, M.C. Alonso, M. Sanchez, M.

J. Correia, M. Criado, A. Sagüés, N. Buenfeld, The steel–concrete interface, Mater. Struct. 50 (2017) 143, https://doi.org/10.1617/s11527-017-1010-1.

[75] U.M. Angst, M. Geiker, M.C. Alonso, R. Polder, O.B. Isgor, B. Elsener, H. Wong, A. Michel, K. Hornborstel, C. Gehlen, R. François, M. Sanchez, M. Criado, H. Sørensen, C. Hansson, R. Pillai, S. Mundra, J. Gulikers, M. Raupach, J. Pacheco, A. Sagüés, The effect of the steel–concrete interface on chloride-induced corrosion initiation in concrete: a critical review by RILEM TC 262-SCI, Mater. Struct. 52 (2019) 88, https://doi.org/10.1617/s11527-019-1387-0.

[76] M. Stefanoni, U.M. Angst, B. Elsener, Electrochemistry and capillary condensation theory reveal the mechanism of corrosion in dense porous media, Sci. Rep. 8 (2018) 7407, https://doi.org/10.1038/s41598-018-25794-x.